OPEN ACCESS



Measuring the Orbits of the Arches and Quintuplet Clusters Using HST and Gaia: Exploring Scenarios for Star Formation near the Galactic Center

Matthew W. Hosek, Jr. 1,4 , Tuan Do 1, Jessica R. Lu 2, Mark R. Morris 1, Andrea M. Ghez 1, Gregory D. Martinez 1, and Jay Anderson 3, Andrea M. Ghez 1, Gregory D. Martinez 1, and

Department of Physics and Astronomy, UCLA, Los Angeles, CA 90095, USA; mwhosek@astro.ucla.edu
 Department of Astronomy, 501 Campbell Hall, University of California, Berkeley, CA, 94720, USA
 Space Telescope Science Institute, 3700 San Martin Drive, Baltimore, MD 21218, USA
 Received 2022 June 7; revised 2022 August 15; accepted 2022 August 16; published 2022 November 3

Abstract

We present new absolute proper-motion measurements for the Arches and Quintuplet clusters, two young massive star clusters near the Galactic center. Using multiepoch HST observations, we construct proper-motion catalogs for the Arches (\sim 35,000 stars) and Quintuplet (\sim 40,000 stars) fields in ICRF coordinates established using stars in common with the Gaia EDR3 catalog. The bulk proper motions of the clusters are measured to be ($\mu_{\alpha*}$, μ_{δ}) = (-0.80 ± 0.032 , -1.89 ± 0.021) mas yr⁻¹ for the Arches and ($\mu_{\alpha*}$, μ_{δ}) = (-0.96 ± 0.032 , -2.29 ± 0.023) mas yr⁻¹ for the Quintuplet, achieving \gtrsim 5× higher precision than past measurements. We place the first constraints on the properties of the cluster orbits that incorporate the uncertainty in their current line-of-sight distances. The clusters will not approach closer than \sim 25 pc to Sgr A*, making it unlikely that they will inspiral into the nuclear star cluster within their lifetime. Further, the cluster orbits are not consistent with being circular; the average value of $r_{\rm apo}/r_{\rm peri}$ is \sim 1.9 (equivalent to an eccentricity of \sim 0.31) for both clusters. Lastly, we find that the clusters do not share a common orbit, challenging one proposed formation scenario in which the clusters formed from molecular clouds on the open stream orbit derived by Kruijssen et al. Meanwhile, our constraints on the birth location and velocity of the clusters offer mild support for a scenario in which the clusters formed via collisions between gas clouds on the x_1 and x_2 bar orbit families.

Unified Astronomy Thesaurus concepts: Galactic center (565); Young star clusters (1833); Star formation (1569); Astrometry (80)

Supporting material: machine-readable tables

1. Introduction

The proximity of the Milky Way Galactic center (GC) offers a unique opportunity to study star formation near a galactic nucleus. The central \sim 500 pc of the Galaxy, known as the Central Molecular Zone (CMZ), hosts two of the most massive young clusters in the Galaxy: the Arches and Quintuplet clusters. With ages less than \sim 5 Myr (Najarro et al. 2004; Martins et al. 2008; Liermann et al. 2012; Clark et al. 2018b, 2018a) and masses of $\sim 10^4 \,\mathrm{M}_\odot$ (Figer et al. 1999a, 1999b; Clarkson et al. 2012), these clusters are the product of recent massive star formation events. They are located at projected distances of $\sim 30 \,\mathrm{pc}$ from the central supermassive black hole (Sgr A*), and, with the exception of the Young Nuclear Cluster immediately surrounding Sgr A*, are the only known young clusters in the region. Since the strong tidal shear in the CMZ is expected to dissolve such clusters on timescales of \$\leq\$20 Myr (Kim et al. 2000; Portegies Zwart et al. 2002), the mechanism(s) that formed the Arches and Quintuplet clusters may have produced additional unobserved clusters in the past and thus play a significant (possibly dominant) role in star formation near the GC.

Original content from this work may be used under the terms of the Creative Commons Attribution 4.0 licence. Any further distribution of this work must maintain attribution to the author(s) and the title of the work, journal citation and DOI.

How the Arches and Quintuplet clusters formed is under debate. One possibility is that the clusters formed from collisions between gas on the " x_1 " and " x_2 " families of orbits found in a barred potential (e.g., Binney et al. 1991). The x_1 orbits, which extend along the major axis of the galactic bar out to ~ 1 kpc, self-intersect as they approach the inner Lindblad resonance of the bar. Gas clouds collide and shock at these locations, lose angular momentum, and begin to fall toward the GC on more radial trajectories. Meanwhile, gas accumulates in the CMZ along the x_2 orbits, which are elongated along the minor axis of the bar with radii of $\sim 0.1-0.2$ kpc. The infalling x_1 gas collides with the x_2 gas, enhancing gas densities and possibly triggering star formation. This behavior is seen in hydrodynamic simulations of large-scale gas flows in the Galaxy (e.g., Sormani et al. 2018; Armillotta et al. 2019; Tress et al. 2020; Armillotta et al. 2020; Salas et al. 2020).

A second possibility is that the clusters formed from molecular clouds on the open stream orbit derived for dense gas in the CMZ by (Kruijssen et al. 2015, hereafter KDL15), without the need for a gas collision. In this "open stream" scenario, cloud collapse is triggered by tidal compression as the natal clouds move through the pericenter passage (Longmore et al. 2013; Kruijssen et al. 2015) or transition into a tidally compressive regime in the gravitational potential (Kruijssen et al. 2019). While this model has been found to be consistent with the observed morphology and kinematics of the CMZ clouds (e.g., Henshaw et al. 2016; Langer et al. 2017; Krieger et al. 2017; Kruijssen et al. 2019), the actual location of several clouds on the proposed orbit is debated (e.g., Butterfield et al. 2018;

⁴ Brinson Prize Fellow.

Tress et al. 2020) and other configurations have been suggested (e.g., two nuclear spirals; Sofue 1995; Ridley et al. 2017).

One way to test these formation scenarios is to determine whether the observed motion and orbital properties of the clusters are consistent with these scenarios. A major challenge in this approach is measuring the absolute proper motions of the clusters, which is difficult due to the lack of observable distant background sources needed to establish an absolute reference frame. Past studies have used the relative proper motion of the clusters compared to the field stars as an approximation for their absolute proper motions (Stolte et al. 2008; Clarkson et al. 2012; Stolte et al. 2014). Recently, the situation has improved with the success of the European Space Agency's Gaia mission, which measures the absolute positions and proper motions of billions of stars across the sky (Gaia Collaboration et al. 2016). While the Arches and Quintuplet cannot be directly observed by Gaia (they are too extinguished at optical wavelengths to be detected), there are several bright foreground stars near the clusters with Gaia measurements that can be used to establish an absolute reference frame, leading to the first measurements of the absolute proper motions of the clusters by Libralato et al. (2020).

A second challenge to this analysis is that the present-day line-of-sight distances ($d_{\rm los}$) of the clusters are not well constrained. As a result, there are many possible orbits that can fit the on-sky position and three-dimensional motion of each cluster (Stolte et al. 2008, 2014; Libralato et al. 2020). This uncertainty must be taken into account in order to place statistical constraints on their orbits, birth locations, and birth velocities. The uncertainties in the cluster ages must be accounted for, as well.

We use Hubble Space Telescope (HST) Wide-Field Camera 3 Infrared Camera (WFC3-IR) observations and the Gaia Early Data Release 3 (EDR3) catalog to measure the absolute proper motions of the Arches and Quintuplet clusters to significantly higher precision then previously achieved. Combining these measurements with radial velocities from the literature, we forward-model the orbits of the clusters while taking the uncertainties in d_{los} , cluster age, and position/motion measurements into account. We calculate probability distributions for the orbital properties, birth positions, and birth velocities of the clusters, and compare them to the predictions of the x_1 – x_2 gas collision and open stream scenarios to evaluate whether they are viable formation mechanisms for the the Arches and Quintuplet clusters.

The paper is organized as follows: In Section 2 we describe the HST observations and astrometric measurements while in Section 3 we explain our methodology for transforming the HST astrometry into the Gaia reference frame and present absolute proper-motion catalogs for the cluster fields. Our measurements of the bulk absolute proper motions of the clusters are reported in Section 4. We detail our approach to forward-modeling the orbits of the clusters in Section 5 and present the corresponding constraints on their orbital properties, birth velocities, and birth velocities in Section 6. We compare our measurements to past work and place them in the context of the proposed cluster formation scenarios in Section 7. Finally, our conclusions are summarized in Section 8.

Table 1HST WFC3-IR Observations

Cluster	Date	GO/PI	Filter	$N_{ m img}$	$t_{ m img}$
Arches	2010.6150	11671/Ghez	F127M	12	599
Arches	2010.6148	11671/Ghez	F139M	10	349
Arches	2010.6043	11671/Ghez	F153M	21	349
Arches	2011.6829	12318/Ghez	F153M	21	349
Arches	2012.6156	12667/Ghez	F153M	21	349
Arches	2016.8009	14613/Lu	F153M	21	349
Quintuplet	2010.6070	11671/Ghez	F127M	12	599
Quintuplet	2010.6060	11671/Ghez	F139M	10	349
Quintuplet	2010.6230	11671/Ghez	F153M	21	349
Quintuplet	2011.6880	12318/Ghez	F153M	21	349
Quintuplet	2012.6130	12667/Ghez	F153M	21	349
Quintuplet	2016.8090	14613/Lu	F153M	21	349

Note. Description of columns. Cluster: cluster observed. Date: Date observed. GO/PI: HST GO number and PI of observations. Filter: WFC3-IR filter used. N_{img} : number of images. t_{img} : integration time per image, in seconds.

2. Observations and Measurements

The Arches and Quintuplet clusters were observed with HST WFC3-IR in 2010, 2011, and 2012 as part of a multicycle GO program, with a fourth epoch of additional data obtained in 2016 (Table 1). The 2010 observations included images in the F127M, F139M, and F153M filters, while additional F153M images were obtained in 2011, 2012, and 2016. The F153M observations were designed to maximize astrometric performance, employing a 21 point subpixel dither pattern in order to fully sample the point-spread function (PSF). In addition, each epoch was observed at the same position angle in order to reduce optical distortion between epochs. Meanwhile, the F127M and F139M observations were designed to obtain stellar photometry to approximately the same depth as the F153M data. These observations provide a field of view of $132'' \times 124''$ for each cluster⁶ with a plate scale of 0."121 pix. The Arches field is centered at $(\alpha(J2000), \delta(J2000)) =$ $(17^{h}45^{m}50^{s}49, = -28^{\circ}49'19''.92)$, while the Quintuplet field is centered at $(\alpha(J2000), \delta(J2000)) = (17^{\text{h}}45^{\text{m}}50^{\text{s}}49 - 28^{\circ}49')$ 19".92). A typical F153M image of each cluster is shown in Figure 1.

Stellar astrometry and photometry are extracted in the same manner as described by Hosek et al. (2019, hereafter H19) and Rui et al. (2019, hereafter R19). Briefly, initial measurements are obtained using the FORTRAN code $img2xym_wfc3ir$, a version of the $img2xym_wFC$ package developed for WFC3-IR (Anderson & King 2006). Stars are iteratively detected and measured using a library of spatially variable PSFs arranged in a 3×3 grid across the field. After the first iteration, a uniform perturbation is applied to the PSF library in order to minimize the residuals of the PSF fit. Subsequent iterations use the perturbed PSF models to extract improved measurements. Within a given epoch, common stars across the images are matched and a first-order polynomial transformation (six free parameters) is used to transform the stellar positions into a common reference frame for that epoch.

⁵ All data used in this paper can also be found in MAST: 10.17909/rgcy-2n46.

Note that this field of view is only slightly larger than that of a single WFC3-IR field, due to the compact dither pattern.

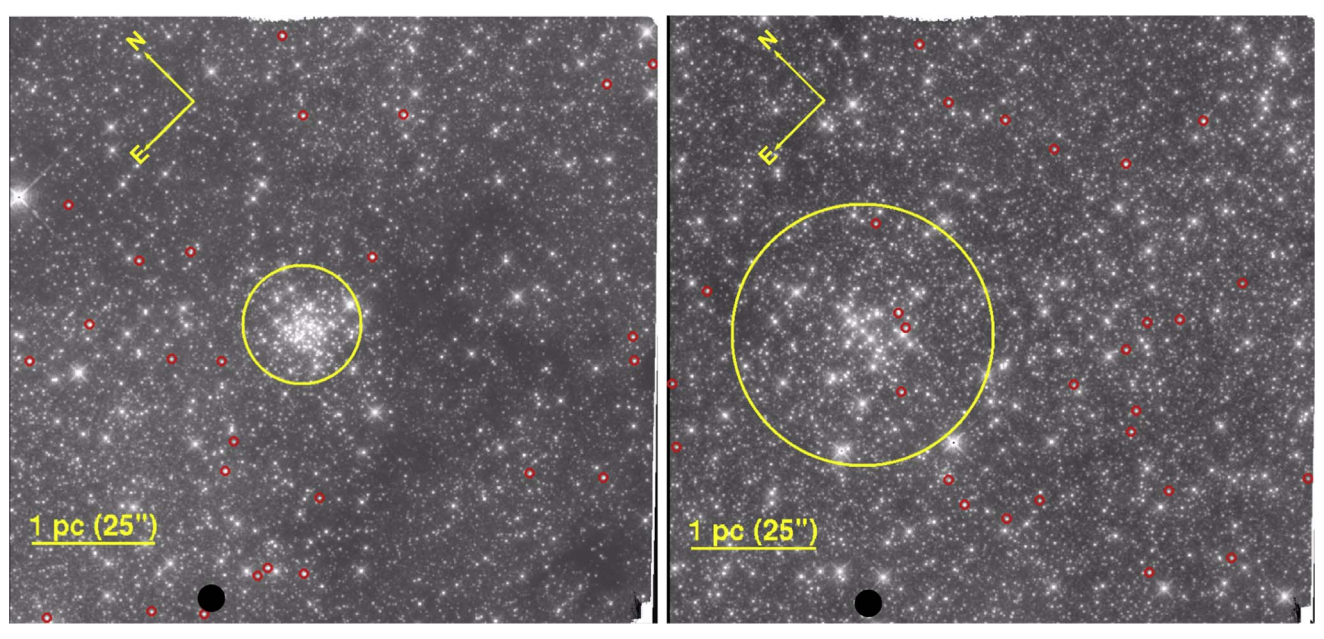


Figure 1. HST WFC3-IR images of the Arches (left) and Quintuplet (right) clusters in the F153M filter with a log stretch. The yellow circle represents the half-light radius of the clusters. We use foreground stars from the Gaia EDR3 catalog (red circles) to establish an absolute reference frame for the HST astrometry.

Next, a master starlist for each epoch is produced using KS2, a FORTRAN code that uses the img2xym_wfc3ir output to detect fainter stars in the field (see Anderson et al. 2008; Bellini et al. 2017, 2018). KS2 uses the transformations to stack the images into a common reference frame. Stars are iteratively detected in the image stack, where the PSF of the detected sources are subtracted in each iteration to allow the detection of fainter stars. Final astrometric and photometric measurements of the stars are made in each individual image at their detected location in the image stack. The astrometric error for each source, σ_{HST} , is calculated as the standard error of the stellar position across all the images in the epoch (e.g., $\sigma_{\rm HST}$ $= \sigma / \sqrt{N_{\text{frames}}}$, where σ is the standard deviation of the positions and N_{frames} is the number of images the star is detected in). Extracted magnitudes are converted from instrumental to Vega magnitudes using the KS2 photometric zeropoints derived in Hosek et al. (2018). These master starlists contain \sim 46,000 stars for the Arches cluster field and \sim 56,000 stars for the Quintuplet cluster field, with a typical depth of F153M \sim 23 mag (95th percentile of the detected magnitudes).

3. HST Absolute Proper Motions

We use the Gaia EDR3 catalog (Gaia Collaboration et al. 2021) to transform the HST astrometry into an absolute reference frame. The Gaia catalog is aligned to the International Celestial Reference Frame (ICRF) using the positions of over 2000 quasars. The resulting Gaia reference frame is found to be consistent with the ICRF at the level of \sim 0.01 mas with a relative rotation of \lesssim 0.01 mas yr⁻¹ (Gaia Collaboration et al. 2021). We ignore this uncertainty in the following analysis since this is well below the best astrometric precision of the HST measurements (\sim 0.3 mas).

3.1. Selecting Gaia Reference Stars

There are a limited number of sources in common between the HST observations and the Gaia EDR3 catalog that are suitable to use to establish an absolute astrometric reference frame (Figure 1). There are several reasons for this: (1) The extremely high extinction toward the GC means that most of the sources detected in the near-infrared HST observations are too faint to be detected in the optical Gaia observations, and so common sources must come from the foreground stellar population; (2) these foreground stars are among the brightest in the HST images and thus may be saturated, reducing their astrometric accuracy; and (3) the fields have significant stellar crowding that can bias astrometric measurements. With this in mind, we make the following set of quality cuts on the Gaia catalog sources in order to identify possible reference stars:

- 1. astrometric_params_solved = 31, indicating that the source has a five-parameter astrometric solution (position, parallax, and proper motion) and a good measurement of the effective wavenumber that is used for the color-dependent PSF correction terms (Lindegren et al. 2021)
- 2. duplicated_source = False, ensuring that no other Gaia sources are within 0.18 (Lindegren et al. 2021)
- 3. parallax_over_error $\geqslant -10$, to eliminate sources with significantly negative (e.g., unphysical) parallaxes (e.g., Arenou et al. 2018)
- 4. astrometric_excess_noise_sig ≤ 2, meaning that no significant excess noise is present in the astrometric solution beyond the statistical errors (Lindegren et al. 2021)
- 5. Gaia G > 13 mag, as the systematic errors in sources brighter than this is not yet well characterized in the EDR3 catalog (Lindegren et al. 2021)
- 6. F153M ≥ 13.8 mag for the HST source matched to the Gaia star, avoiding the regime where the HST astrometric error begins to increase due to saturation.

After these cuts, 30 potential reference stars remain in the Arches field and 41 potential reference stars remain in the Quintuplet field. As a final check of the astrometric quality of the reference stars, initial transformations are calculated using the procedure outlined in Section 3.2 to convert the HST

astrometry into the Gaia reference frame. Reference stars that have transformed HST positions or proper motions that are discrepant by $\geqslant 3\sigma$ from their Gaia EDR3 values (where σ is defined as the quadratic sum of the astrometric errors from HST and Gaia) are iteratively removed from the sample, where the largest outlier is removed in each iteration and the transformations are recalculated to determine if the remaining outliers are still discrepant. This process is repeated until no more 3σ outliers exist. Stars removed by this procedure are often found in close proximity to the diffraction spikes of bright stars or near the edge of the HST field. In total, 4 stars are removed from the Arches reference star sample and 13 reference sources are removed from the Quintuplet reference star sample via this process.

Ultimately, 26 Gaia sources are used as reference stars in the Arches field and 28 Gaia sources are used as reference stars in the Quintuplet field. The locations of these reference stars are shown in Figure 1.

3.2. Transforming HST Astrometry into the Gaia Reference Frame

We transform the HST master starlists into the Gaia EDR3 reference frame on an epoch-by-epoch basis using the reference stars identified in Section 3.1. First, the Gaia EDR3 proper motions are used to calculate the expected positions of the reference stars at a given HST epoch, with the astrometric uncertainty propagated accordingly. Next, five of the reference stars are matched to their HST counterparts by eye, and an initial transformation from the HST pixel coordinates into the Gaia coordinates is calculated via a first-order polynomial (six free parameters). This transformation is applied to the entire HST starlist to provide an initial estimate of their positions in the Gaia frame. The full list of reference stars is then compared to the transformed HST positions, and matches are identified as sources with positions that are consistent within 80 mas.

The set of matched reference stars is used to calculate the final transformation from HST pixels into Gaia coordinates via a second-order polynomial transformation (12 free parameters 7). Each reference star is weighted by $1/\sigma_{\rm tot}^2$, where $\sigma_{\rm tot}$ is the quadratic sum of the intrinsic HST and Gaia astrometric errors for that source. We refer to the transformed HST positions as the "HST-Gaia reference frame," which is aligned with the ICRF via the Gaia EDR3 reference frame.

The uncertainty of the transformation into the HST-Gaia reference frame is calculated via a full sample bootstrap over the reference stars. We resample the reference stars (with replacement) 100 times and recalculate the second-order polynomial transformation for each sample. The resulting transformations are then applied to the original HST master starlists. The transformation error ($\sigma_{\rm trans}$) for each star is calculated as the standard deviation of its transformed position across all the bootstrap iterations. This is combined with the intrinsic astrometric error ($\sigma_{\rm HST}$) to get the total astrometric error $\sigma_{\rm ast}$:

$$\sigma_{\rm ast} = \sqrt{\sigma_{\rm HST}^2 + \sigma_{\rm trans}^2}.$$
 (1)

Figure 2 shows σ_{ast} as a function of F153M magnitude for the Arches cluster in the 2012 epoch, which is representative of

To assess the performance of the HST-Gaia reference frame, we compare the proper motions of the reference stars derived from the transformed HST astrometry to their corresponding values in the Gaia EDR3 catalog (Figure 3). The overall accuracy and uncertainty of the HST-Gaia reference frame is defined as the error-weighted average of the proper-motion differences $(\Delta\mu_{\alpha^*},\ \Delta\mu_{\delta})$ and the corresponding error in the weighted average. We obtain $(\Delta\mu_{\alpha^*},\ \Delta\mu_{\delta})=(-0.027\pm0.03,\ -0.004\pm0.02)$ mas yr $^{-1}$ for the Arches and $(\Delta\mu_{\alpha^*},\ \Delta\mu_{\delta})=(-0.006\pm0.030,\ -0.004\pm0.02)$ mas yr $^{-1}$ for the Quintuplet. This indicates that the HST-Gaia and Gaia EDR3 reference frames are consistent within 0.03 mas yr $^{-1}$ and 0.02 mas yr $^{-1}$ in the μ_{α^*} and μ_{δ} directions, respectively. As discussed in Section 4, the uncertainty in the HST-Gaia reference frame is the largest source of uncertainty in the absolute proper motions of the clusters.

3.3. Final Proper-motion Catalogs

Proper motions are calculated from linear fits of the R.A. \cdot cos(decl.) and decl. positions (hereafter α^* and δ) as a function of time for all stars detected in at least three epochs:

$$\alpha^* = \alpha_0^* + \mu_{\alpha^*}(t - t_0), \tag{2}$$

$$\delta = \delta_0 + \mu_\delta(t - t_0),\tag{3}$$

where (α^*, δ) is the observed position at time t, (α_0^*, δ_0) are the fitted (α^*, δ) position at t_0 , and $(\mu_{\alpha^*}, \mu_{\delta})$ are the corresponding proper motions. t_0 is the astrometric error-weighted average time of the data points, and each data point is weighted by $1/\sigma_{\rm ast}^2$ in the fit. The resulting proper-motion catalogs contain 40,932 stars for the Arches cluster field and 46,087 stars for the Quintuplet cluster field. Proper-motion uncertainties as a function of magnitude are shown in Figure 2. The best-measured stars have proper-motion uncertainties of \sim 0.07 mas yr⁻¹, which is \sim 2× higher than the errors achieved by H19 and R19. As discussed in Section 3.2, this is due to the penalty in astrometric precision incurred when transforming into an absolute reference frame.

We apply two quality cuts to the proper-motion catalogs for the final analysis. First, we remove stars with proper-motion errors larger than $1.4 \,\mathrm{mas} \,\mathrm{yr}^{-1}$ in order to remove stars with large uncertainties. Then, we eliminate stars with absolute proper-motion values larger than 99.7% of the rest of the sample, as these sources are either bad measurements or fast-moving foreground stars that do not represent the bulk field and cluster stellar populations. After these cuts, 34,600 stars remain in the Arches cluster sample (\sim 85% of the original catalog) and 40,499 stars remain in the Quintuplet cluster sample (\sim 88% of

Higher-order polynomial transformations did not yield significant improvement compared to the second-order polynomial transformations and thus were deemed to be unnecessary.

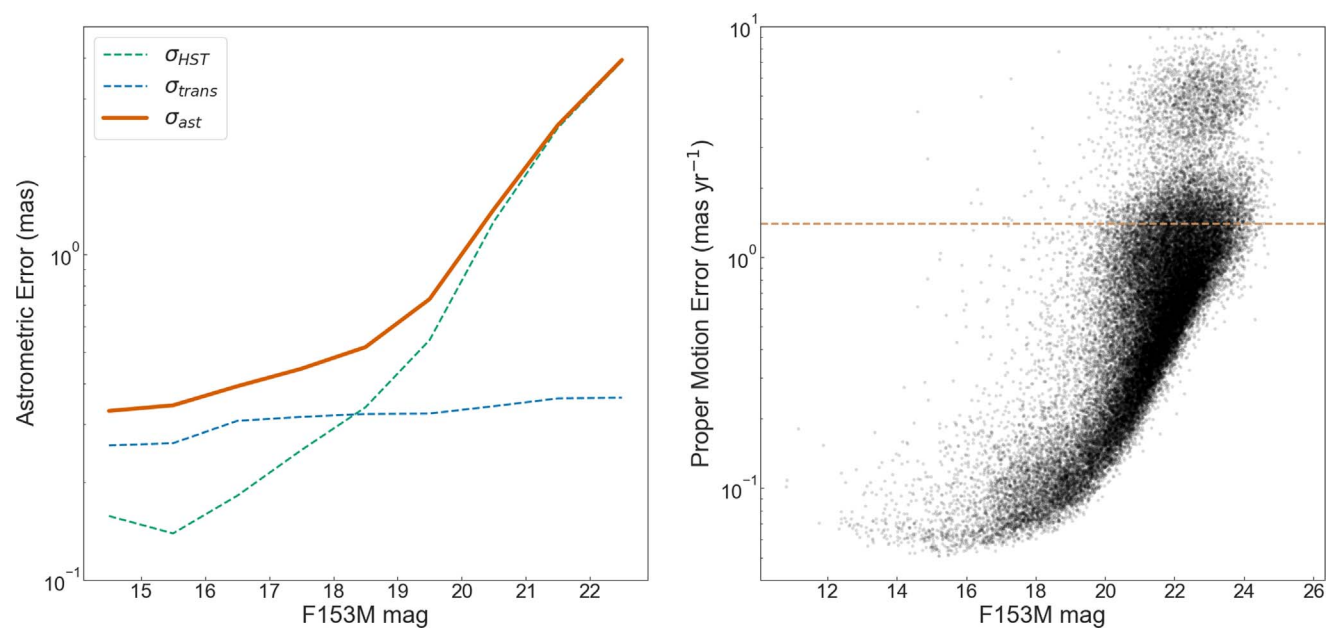


Figure 2. Left: the total astrometric error (σ_{ast} ; red solid line), intrinsic HST astrometric error (σ_{HST} ; green dotted line), and transformation error (σ_{trans} ; blue dotted line) as a function of magnitude for the Arches cluster field in the 2012 epoch. The best-measured stars have typical σ_{ast} values of \sim 0.3 mas, which is dominated by σ_{trans} . Right: proper-motion error as a function of magnitude for the Arches cluster field. Stars with errors larger than 1.4 mas yr⁻¹ (dashed line) are excluded from the analysis. We achieve a precision of \sim 0.07 mas yr⁻¹ for the brightest nonsaturated stars. We achieve similar astrometric performance for the Quintuplet cluster field.

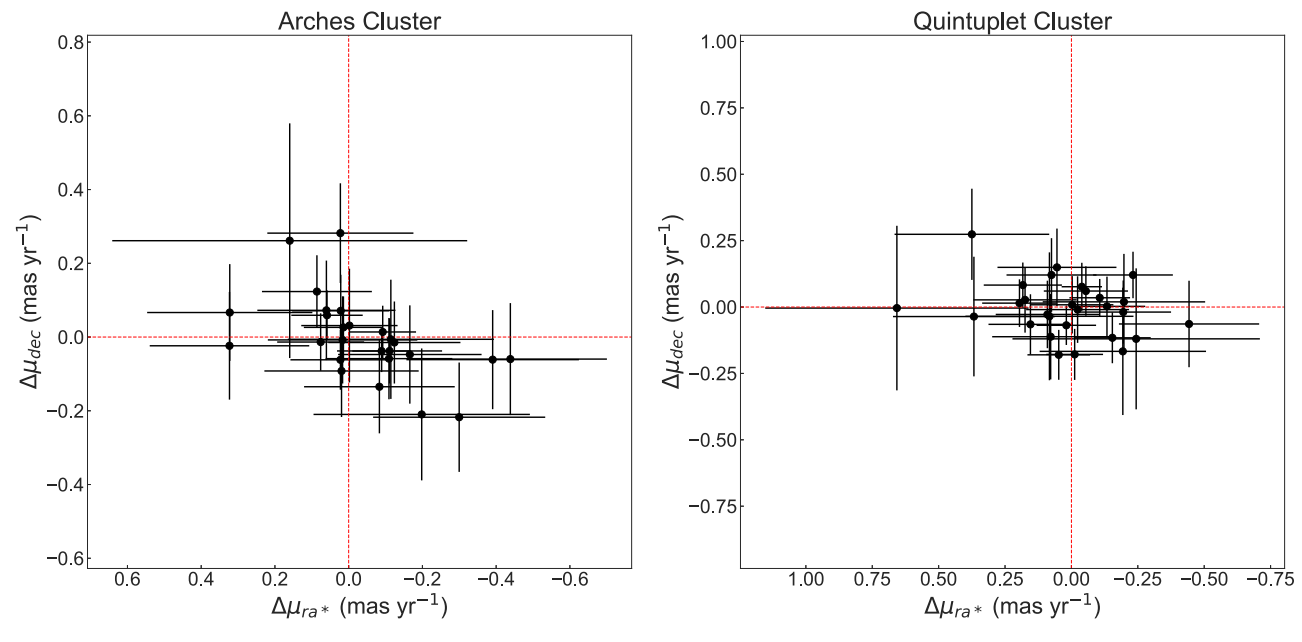


Figure 3. The proper-motion differences of the reference stars between the HST-Gaia and Gaia EDR3 reference frames for the Arches (left) and Quintuplet (right) fields. We find that the HST-Gaia reference frame is consistent with the Gaia EDR3 reference frame to ≤ 0.03 mas yr^{-1} . This is the dominant source of error in our absolute proper-motion measurements of the Arches and Quintuplet clusters.

the original catalog). Summary statistics for the proper-motion catalogs are provided in Table 2, and samples of the Arches and Quintuplet catalogs are shown in Tables 3 and 4. Full proper-motion catalogs for both cluster fields are provided in machine-readable form with this work.

We perform several checks of the proper motions in Appendix A, examining the χ^2 distribution of the fits and the average astrometric residuals in each epoch. In summary, we find that the χ^2 distributions are similar to their theoretical distribution, indicating that the proper-motion fit residuals are well characterized by the astrometric errors. We also find that

the average astrometric residuals for each epoch (which we refer to as the residual distortion) is less than half of the astrometric error for bright stars and thus do not significantly impact our results.

4. The Absolute Proper Motion of the Arches and Quintuplet Clusters

Star cluster members share a common proper motion on the sky and thus form a distinct concentration in proper-motion space. As a result, proper motions provide a reliable method for

 Table 2

 HST Proper-motion Catalog: Summary Statistics

Cluster	$N_{ m stars}$	Depth F153M mag	$\sigma_{ m ast}$ mas	$\frac{\overline{\sigma_{\rm pm}}}{{ m mas yr}^{-1}}$	$\overline{\sigma_{ m mag}}$ mag
Arches	34,600	23.04	0.18	0.07	0.01
Quintuplet	40.499	22.60	0.25	0.09	

Note. Description of columns. N_{stars} : number of stars in the catalog. Depth: 95th percentile of F153M magnitudes. $\overline{\sigma_{ast}}$: median error in position for propermotion fits for stars with F153M \leq 16 mag. $\overline{\sigma_{pm}}$: median error in propermotion for proper-motion fits for stars with F153M \leq 16 mag. $\overline{\sigma_{mag}}$: median F153M photometric error for F153M \leq 16 mag.

identifying stars in the Arches and Quintuplet clusters (e.g., Stolte et al. 2008; Clarkson et al. 2012; Hußmann et al. 2012; Hosek et al. 2015), a difficult task to do from photometry alone due to severe differential extinction across the field. Following H19 and R19, we use a Gaussian Mixture Model (GMM) to model the proper-motion distribution of the cluster and field star populations. Because our proper motions are tied to the Gaia EDR3 reference frame, the center of the Gaussian distribution that describes the cluster population corresponds to the bulk proper motion of the cluster in the ICRF. In addition, a cluster membership probability for each star is calculated using the GMM and is included in the proper-motion catalogs (Tables 3 and 4). Details of the GMM analysis and the best-fit models are provided in Appendix B.

The distribution of cluster and field star proper motions in each field is shown in Figure 4. The bulk proper motions of the clusters in ICRF are $(\mu_{\alpha*},\,\mu_{\delta})_{\rm ICRF}=(-0.80\pm0.032,\,-1.89\pm0.021)\,{\rm mas}\,{\rm yr}^{-1}$ for the Arches and $(\mu_{\alpha*},\,\mu_{\delta})_{\rm ICRF}=(-0.96\pm0.032,\,-2.29\pm0.023)\,{\rm mas}\,{\rm yr}^{-1}$ for the Quintuplet. The uncertainty in this measurement is the quadratic sum of the uncertainty in the centroid of the cluster Gaussian and the uncertainty in the reference frame (Section 3.2). The reference frame dominates the uncertainty in this measurement.

The cluster proper motion in ICRF is a combination of the cluster's motion in the rest frame of the galaxy (i.e., its motion relative to Sgr A*, hereafter referred to as the "Sgr A*-at-Rest" frame) as well as the reflex motion from the Sun's orbit in the Galaxy. To calculate the cluster motion in the Sgr A*-at-Rest frame, we subtract the observed proper motion of Sgr A* in the ICRF (($\mu_{\alpha*}$, μ_{δ})_{ICRF} = (-3.156 ± 0.006, -5.585 +/- 0.010) mas yr $^{-1}$; Reid & Brunthaler 2020), which we assume is induced entirely by the solar orbital motion. The motions of the clusters in the Sgr A*-at-Rest frame are thus ($\mu_{\alpha*}$, μ_{δ})_{int} = (2.36 ± 0.033, 3.70 ± 0.024) mas yr $^{-1}$ for the Arches and ($\mu_{\alpha*}$, μ_{δ})_{int} = (2.20 ± 0.032, 3.30 ± 0.025) masyr $^{-1}$ for the Quintuplet.

A summary of the these proper-motion measurements is provided in Table 5.

5. Modeling the Cluster Orbits

To constrain the orbital properties of the Arches and Quintuplet clusters, we evaluate which orbits can reproduce their observed present-day positions and motions within the uncertainties. The probability of a given orbit model θ is calculated via the Bayes equation:

$$P(\theta|\mathbf{x}) = \frac{P(\mathbf{x}|\theta)P(\theta)}{P(\mathbf{x})},\tag{4}$$

where x is a vector representing the observed position and motion of the cluster in galactic longitude coordinates ($x = \{l, b, d_{los}, \mu_{l^*}, \mu_b, \nu_{los}\}$, where l and b are the galactic longitude and latitude, d_{los} is the line-of-sight distance, μ_{l^*} , μ_b are the proper motion in galactic longitude and latitude, and ν_{los} is radial velocity). $P(x|\theta)$ is the likelihood of observing x given θ , $P(\theta)$ is the prior probability on the free parameters in θ , and P(x) is the evidence.

The orbit model θ is described in Section 5.1 while the observational constraints on the cluster positions and motions are given in Section 5.2. The likelihood equation used to compare θ to the observations is defined in Section 5.3, while the adopted gravitational potential for the GC is discussed in Section 5.4.

5.1. The Orbit Model

We adopt an orbit model θ with seven free parameters. Six of the free parameters describe the birth position (x_b, y_b, z_b) and birth velocity (vx_b, vy_b, vz_b) of the cluster in Galactocentric coordinates. The final model parameter is the current cluster age t_{clust} .

The birth positions and velocities have uniform priors with bounds based on the assumption that the clusters formed within the CMZ. The priors on x_b , y_b , and z_b encompass the spatial distribution of gas observed in the region. x_b and y_b , which define the location on the galactic plane, conservatively extend ± 300 pc from Sgr A* (e.g., Morris & Serabyn 1996). z_b , which defines the location perpendicular to the galactic plane, spans ± 60 pc, corresponding to approximately twice the observed height of the distribution of dense gas in the region (e.g., Molinari et al. 2011). Similarly, the priors for vx_b and vy_b span $\pm 300 \, \mathrm{km \, s^{-1}}$, enveloping the range of observed line-ofsight velocities of gas within $|l| < 2^{\circ}$ (corresponding to a spatial scale of $|l| \lesssim 280 \,\mathrm{pc}$; Bitran et al. 1997; Dame et al. 2001). The prior for vz_b also covers $\pm 300 \,\mathrm{km \, s^{-1}}$, allowing for significant vertical oscillations from the Galactic Plane. These priors are intentionally broad so that the resulting constraints on the birth positions and velocities (and thus orbits) of the clusters are as agnostic as possible to proposed formation mechanisms, and thus can be used to examine the viability of such mechanisms (Section 7.2). Finally, the priors for t_{clust} come from constraints in the literature, which generally fall between 2.5–3.5 Myr for the Arches (e.g., Najarro et al. 2004; Martins et al. 2008; Clark et al. 2018a) and 3-5 Myr for the Quintuplet (e.g., Liermann et al. 2012; Hußmann et al. 2012; Clark et al. 2018b). Thus, we adopt Gaussian priors for t_{clust} with means and standard deviations of $3 \pm 0.5 \, \text{Myr}$ and 4 ± 1 Myr for the Arches and Quintuplet, respectively. The model parameters and priors are summarized in Table 6.

The parameter space is explored using the multimodal nested sampling algorithm Multinest (Feroz & Hobson 2008; Feroz et al. 2009), called by the Python wrapper code PyMultinest (Buchner et al. 2014). Values for the free parameters are drawn from the priors and the corresponding orbit is integrated in the GC gravitational potential to $t_{\rm clust}$ using galpy (Bovy 2015). This makes a prediction for what

This is a left-handed coordinate system centered on Sgr A*, where $x = D \cdot \cos l \cdot \cos b$, $y = D \cdot \sin l \cdot \cos b$, and $z = D \cdot \sin b$, where D is the distance to the object. x is positive in the line-of-sight direction from the GC toward the Sun, y is positive in the Galactic Plane toward positive l, and z is positive toward the North Galactic Pole (J. Bovy 2022, in preparation).

Name	F127M mag	$\sigma_{ m F127M}$ mag	F139M mag	$\sigma_{ m F139M}$ mag	F153M mag	$\sigma_{ m F153M}$ mag	$lpha_0^{*a}$	$\sigma_{\alpha_0^*}^*_{_{_{_{_{_{_{_{_{_{_{_{_{_{_{_{_{_{_{$	$\delta_0^{\mathbf{a}}$	σ_{δ_0}	$\max_{\mathrm{mas}\ \mathrm{yr}^{-1}}^{\mu_{\alpha^*}}$	$\max_{\alpha^*} \frac{\sigma_{\mu_{\alpha^*}}}{\text{mas yr}^{-1}}$	μ_{δ} mas yr $^{-1}$	$\max_{}^{\sigma_{\mu_{\delta}}} \operatorname{yr}^{-1}$	t ₀ year	$N_{ m obs}$	$\chi^2_{\alpha^*}$	χ^2_δ	$P_{ m clust}$
A0000001	11.41	0.02	11.12	0.01	10.81	0.02	-11.38042	0.00024	-2.89786	0.00023	0.23	0.11	-1.01	0.10	2013.0250	4	0.46	0.06	0.00
A0000002	11.41	0.01	11.13	0.01	10.85	0.01	36.87441	0.00025	26.16057	0.00024	0.17	0.11	-4.78	0.10	2012.9390	4	1.69	0.85	0.00
A0000003	11.85	0.03	11.53	0.02	11.15	0.02	-92.22162	0.00040	-6.60737	0.00054	2.41	0.16	-0.55	0.20	2013.4949	4	0.11	0.54	0.00
A0000004	14.27	0.01	13.60	0.01	11.73	0.01	-84.04126	0.00033	-15.98480	0.00048	-0.53	0.13	-2.65	0.18	2013.5663	4	0.13	0.23	0.00
A0000005	12.43	0.01	12.10	0.01	11.76	0.01	0.49685	0.00018	-21.67100	0.00016	-2.80	0.08	-3.48	0.06	2013.0293	4	0.33	0.38	0.00

Notes. Description of columns. Name: star name. F127M, F139M, F153M: mags in corresponding filters (Vega). σ_{F127M} , σ_{F139M} , σ_{F133M} : error in corresponding mags. α_0^* , δ_0 : α^* and δ positions at t_0 . $\sigma_{\alpha_0^*}$, σ_{δ_0} : error in α_0^* and δ_0 . μ_{α^*} , μ_{δ_0} : proper motions in α^* and δ_0 . μ_{α^*} , $\sigma_{\mu_{\delta_0}}$: error in μ_{α^*} and μ_{δ} . t_0 : reference time for proper-motion fits (Equations (2) and (3)). N_{obs} : Number of epochs observed. χ_{α}^2 , χ_{δ}^2 : χ^2 values for μ_{α^*} and μ_{δ} fits. P_{clust} : cluster membership probability calculated via the GMM.

(This table is available in its entirety in machine-readable form.)

^a Positions are relative to $(\alpha(J2000), \delta(J2000)) = (17^{h}45^{m}50.65020, -28^{\circ}49'19.51468)14$.

 Table 4

 Absolute Proper Motion Catalog of the Quintuplet Cluster

Name	F127M mag	σ _{F127M} mag	F139M mag	$\sigma_{ m F139M}$ mag	F153M mag	$\sigma_{ m F153M}$ mag	$lpha_0^{*a}$	$\sigma_{lpha_0^*}$	δ_0^{a}	σ_{δ_0} ,,	$\max_{\mathrm{mas}\ \mathrm{yr}^{-1}}^{\mu_{\alpha^*}}$	$\max_{\mathbf{mas}\ \mathbf{yr}^{-1}}^{\sigma_{\mu_{\Omega^*}}}$	μ_{δ} mas yr $^{-1}$	$\max_{}^{\sigma_{\mu_{\delta}}} \operatorname{yr}^{-1}$	t ₀ year	$N_{ m obs}$	$\chi^2_{\alpha^*}$	χ^2_{δ}	$P_{ m clust}$
Q0000001	13.71	0.02	12.94	0.02	11.03	0.02	-21.16637	0.00048	-91.72974	0.00052	-1.96	0.19	-3.84	0.21	2013.4494	4	5.70	1.62	0.00
Q0000002	13.16	0.00	12.14	0.01	11.15	0.01	5.61601	0.00022	1.70905	0.00025	-0.98	0.09	-2.36	0.09	2013.4065	4	1.17	0.90	0.93
Q0000003	13.38	0.01	12.71	0.01	11.20	0.01	35.65604	0.00035	-35.15230	0.00045	-0.26	0.14	-5.52	0.16	2013.7870	4	1.76	0.61	0.00
Q0000004	13.52	0.01	12.38	0.02	11.28	0.02	-23.11858	0.00034	38.75195	0.00039	-1.18	0.14	-2.23	0.15	2013.5401	4	0.10	0.11	0.80
Q0000005	13.40	0.01	12.38	0.00	11.36	0.02	10.38729	0.00027	18.52431	0.00033	-0.99	0.12	-2.46	0.12	2013.2733	4	0.15	0.74	0.86

Notes. Description of columns: Name: star name, F127M, F139M, F153M: mags in corresponding filters (Vega), σ_{F127M} , σ_{F139M} , σ_{F133M} : error in corresponding mags, α_0^* , δ_0 : α^* and δ positions at t_0 , $\sigma_{\alpha_0^*}$, σ_{δ_0} : error in α_0^* and δ_0 , μ_{α^*} , μ_{δ_0} : proper motions in α^* and δ , $\sigma_{\mu_{\alpha^*}}$, $\sigma_{\mu_{\delta_0}}$: error in μ_{α^*} and μ_{δ} , t_0 : reference time for proper motion fits (Eqns. (**), (**)), N_{obs} : Number of epochs observed, $\chi_{\alpha^*}^2$, χ_{δ}^2 : χ^2 values for μ_{α^*} and μ_{δ} fits, P_{clust} : cluster membership probability calculated via the GMM.

(This table is available in its entirety in machine-readable form.)

^a Positions are relative to $(\alpha(J2000), \delta(J2000)) = (17^{h}46^{m}14.68579, -28^{\circ}49'38.''99169).$

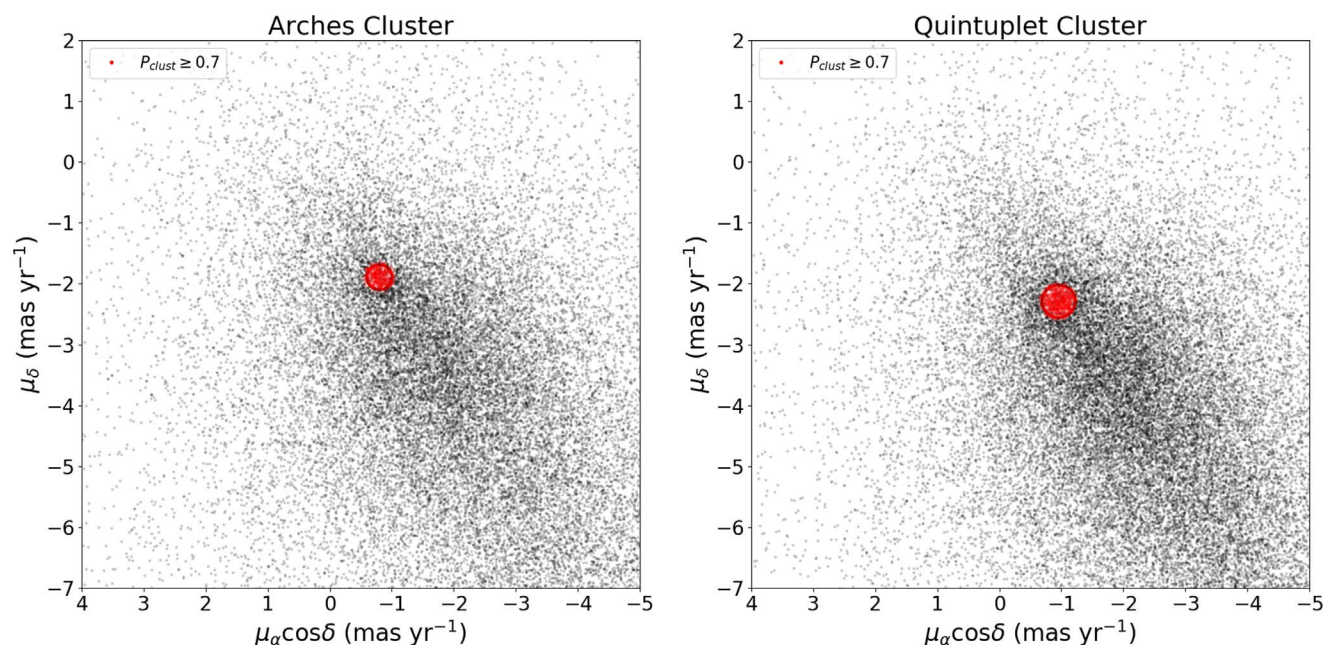


Figure 4. Proper motions of stars in the Arches (left) and Quintuplet (right) fields. Cluster members form a concentrated distribution relative to the field stars. In each plot, the red circle represents the 2σ probability contour of the cluster Gaussian in the GMM and stars with cluster membership probabilities greater than or equal to 0.7 are shown as red points. The velocity centroid of the cluster Gaussian represents the cluster's bulk proper motion in the HST-Gaia reference frame, which is tied to ICRF.

Table 5
Absolute Proper Motions of the Clusters

Cluster	Ref Frame	$_{ m mas~yr^{-1}}^{\mu_{lpha^*}}$	μ_{δ} mas yr $^{-1}$
Arches	ICRF	-0.80 ± 0.032	-1.89 ± 0.021
Arches	Sgr A*-at-Rest	2.36 ± 0.033	3.70 ± 0.024
Quintuplet	ICRF	-0.96 ± 0.032	-2.29 ± 0.023
Quintuplet	Sgr A*-at-Rest	2.20 ± 0.032	3.30 ± 0.025

Note. Description of columns. Ref frame: reference frame of the measurement. μ_{α^*} : proper motion in α^* . μ_{δ} : proper motion in δ .

Table 6Orbit Model: Parameters and Priors

Parameter	Arches Prior	Quintuplet Prior	Units
x_b	U(-300, 300)	U(-300, 300)	pc
y_b	U(-300, 300)	U(-300, 300)	pc
Z_b	U(-60, 60)	U(-60, 60)	pc
vx_b	U(-300, 300)	U(-300, 300)	$\mathrm{km}\ \mathrm{s}^{-1}$
vy_b	U(-300, 300)	U(-300, 300)	${\rm km~s^{-1}}$
vz_b	U(-300, 300)	U(-300, 300)	${\rm km~s^{-1}}$
$t_{ m clust}$	G(6.48, 0.07)	G(6.60, 0.10)	log(years)

Note. Uniform distributions: U(min, max), where min and max are bounds of the distribution; Gaussian distributions: $G(\mu, \sigma)$, where μ is the mean and σ is the standard deviation.

the present-day cluster position and velocity should be in Galactocentric coordinates (e.g., physical units relative to Sgr A*).

5.2. Observational Constraints

To define l, b, μ_{l^*} , and μ_b for x in Equation (4), we convert our results from Section 4 into Galactic coordinates. To calculate μ_{l^*} and μ_b , the $(\mu_{\alpha^*}, \mu_{\delta})_{\text{ICRF}}$ proper motions are

rotated clockwise by an angle of 90°–31°.40 = 58°.60, where 31°.40 is the position angle of the Galactic Plane (Reid & Brunthaler 2004). Following Libralato et al. (2020), we use a Monte Carlo approach to propagate the proper-motion uncertainties through the rotation.

The position of each cluster is calculated from the median (α_0^*, δ_0) position of all stars with cluster membership probabilities $\geqslant 0.7$ in the proper-motion catalogs. This represents the cluster position at 2013.0750 for the Arches and 2013.3530 for the Quintuplet. These positions are transformed into (l, b) using the astropy SkyCoord package (Astropy Collaboration et al. 2013, 2018). The uncertainty in l and b is conservatively estimated to be the half-light radii for the clusters measured as by Hosek et al. (2015) and Rui et al. (2019).

Constraints on $v_{\rm los}$ and $d_{\rm los}$ are taken from the literature. The heliocentric $v_{\rm los}$ of the clusters are measured via spectroscopic studies of the brightest cluster members (Figer et al. 2002; Liermann et al. 2009). Meanwhile, $d_{\rm los}$ is allowed to range $\pm 300~{\rm pc}$ from Sgr A*, making it the weakest of the observational constraints.

This is justified by evidence that the clusters currently reside within the CMZ, such as the ionization of the nearby Arched Filaments and Sickle structures (e.g., Lang et al. 1997, 2001; Simpson et al. 2007; Wang et al. 2010), the orientation of the surrounding ionized cloud edges and gas pillars (Stolte et al. 2014), and the measured trends in gas and dust infrared luminosity and temperatures in the region relative to the

⁹ We take 5000 random samples from Gaussian distributions describing the equatorial proper motions, with the mean and standard deviation of each Gaussian equal to the measured proper motion and its uncertainty, respectively. We then rotate each sample into Galactic coordinates as described here and then take the standard deviation of the rotated coordinates to be the corresponding uncertainty in galactic coordinates.

 $^{^{10}}$ These times represent the median t_0 for the proper-motion fits for the stars used in this calculation.

 Table 7

 Observational Constraints on the Present-day Cluster Positions and Motions

		Arche	es Cluster	Quint	ıplet Cluster
Parameter	Units	Value	Reference	Value	Reference
l	deg	0.1230 ± 0.003	This work	0.1640 ± 0.005	This work
b	deg	0.0175 ± 0.003	This work	-0.0602 ± 0.005	This work
μ_{l*}	mas yr ⁻¹	-2.03 ± 0.025	This work	-2.45 ± 0.026	This work
μ_b	mas yr ⁻¹	-0.30 ± 0.029	This work	-0.37 ± 0.029	This work
d_{los}	pc	±300	see Section 5.2	±300	see Section 5.2
$v_{ m los}$	$\rm km~s^{-1}$	95 ± 8	Figer et al. (2002)	102 ± 2	Liermann et al. (2009

Note. Description of parameters. (l, b) = galactic longitude and latitude (ICRF coordinates. t = 2013.0750 for Arches, t = 2013.3530 for Quintuplet), $d_{\text{los}} = \text{the line-of-sight distance relative to Sgr A*}$. $(\mu_{l^*}, \mu_{b}) = \text{proper motion in galactic longitude}$ and latitude (ICRF coordinates). $v_{\text{los}} = \text{heliocentric line-of-sight velocity}$.

clusters (e.g., Cotera et al. 2005; Hankins et al. 2017). It has also been suggested that diffuse X-ray emission detected near the Arches cluster may be a bow shock due to the cluster colliding with a surrounding molecular cloud (e.g., Wang et al. 2006). However, the localized position of the clusters within the CMZ has not yet been determined.

A summary of the observational constraints used to define x is provided in Table 7.

5.3. Evaluating the Likelihood

The orbit model makes a prediction of the present-day position and motion of the cluster in Galactocentric coordinates, which are in physical units relative to Sgr A* (pc, km s⁻¹). These predictions must be converted into observable units in order to compare to the observed values in Table 7 (deg, mas yr⁻¹ in Galactic coordinates). To convert from (y, z) to (l, b), we assume that the distance between Earth and Sgr A* (R_0) is 8090 ± 140 pc (e.g., the average value and spread between different estimates of R_0 in the literature; Do et al. 2019; Gravity Collaboration et al. 2022) and that the ICRF position of Sgr A* is $(l, b) = (-0.05576, -0.04617)^{\circ}$ (Reid & Brunthaler 2004). Similarly, to convert from (vy, vz)to (μ_{l*}, μ_b) we use the same R_0 and assume an ICRF proper motion for Sgr A* of $(\mu_{l*}, \mu_b) = (-6.411, -0.219)$ mas yr⁻¹ (Reid & Brunthaler 2020). Finally, we convert vx into heliocentric v_{los} by adopting a heliocentric radial velocity for Sgr A* of $-11.1 \pm 1.2 \,\mathrm{km \, s}^{-1}$ (Schönrich et al. 2010), where the uncertainty is the quadratic sum of reported statistical and statistical uncertainties.

We define the likelihood of a given orbit model as

$$P(\mathbf{x}|\theta) = \prod_{i \neq d_{\text{los}}} \exp\left(-\frac{(x_{i,\text{obs}} - x_{i,\theta})^2}{2(\sigma_{x_{i,\text{obs}}}^2 + \sigma_{x_{i,\theta}}^2)}\right) \psi(d_{\text{los},\theta}),$$
(5)

$$\psi(d_{\log,\theta}) = \begin{cases} \frac{1}{600} & |d_{\log,\theta}| \le 300\\ -\infty & |d_{\log,\theta}| > 300 \end{cases}$$
(6)

The first term in Equation (5) applies to all dimensions of x except for d_{los} . Within this term, $x_{i,obs}$ and $\sigma_{x_{i,obs}}$ are the observed value and uncertainty of the ith dimension of x, respectively, $x_{i,\theta}$ is the predicted value for the ith dimension from θ , and $\sigma_{x_{i,\theta}}$ is the uncertainty in $x_{i,\theta}$ incurred when

converting from physical to observed units due to the uncertainties in R_0 and the radial velocity of Sgr A*.

The second term is a piecewise function that only depends on the current line-of-sight distance of the cluster predicted by the orbit model, $d_{\text{los},\theta}$. If $|d_{\text{los},\theta}| > 300 \, \text{pc}$, then it forces the likelihood to be $-\infty$ since this would violate the constraint that the cluster is currently within the CMZ. If $|d_{\text{los},\theta}| \leq 300 \, \text{pc}$, then the second term is a constant value of 1/600, corresponding to a uniform probability distribution spanning $\pm 300 \, \text{pc}$. Thus, as long as $|d_{\text{los},\theta}| \leq 300 \, \text{pc}$, this parameter does not impact the relative likelihood between orbit models.

5.4. GC Gravitational Potential

For the orbit integration, we adopt the same gravitational potential as KDL15, namely an axisymmetric potential based on the enclosed mass distribution from Launhardt et al. (2002) but flattened in the z direction by a factor $q_{\phi}=0.63$ (see Appendix D.1 for additional details). However, the GC gravitational potential is uncertain, and alternative potentials have been proposed (e.g., Sormani et al. 2020a). We explore the impact of different gravitational potentials on our results in Section 7.4.

We note that the adopted gravitational potential (as well as the alternative potentials examined in Section 7.4) is axisymmetric and thus ignores the nonaxisymmetric component of the potential due to the Galactic bar. However, for the range of galactic radii considered in this analysis ($r \lesssim 300\,\mathrm{pc}$) the potential is dominated by the nuclear star cluster (NSC) and nuclear stellar disk (NSD) (e.g., Launhardt et al. 2002). The observed properties of these structures appear to be well reproduced by axisymmetric models (Gerhard & Martinez-Valpuesta 2012; Chatzopoulos et al. 2015; Sormani et al. 2022). Thus, the assumption of an axisymmetric potential is adequate for this analysis, especially for the short timescales under consideration ($\lesssim 5\,\mathrm{Myr}$).

6. The Orbits of the Arches and Quintuplet Clusters

For both clusters, the posterior probability distributions for θ are bimodal and show significant degeneracies. Orbits drawn from the two solution modes for the Arches and Quintuplet are shown in Figures 5 and 6, respectively. The main feature distinguishing the modes is the direction of the orbit. As viewed from the North Galactic Pole (e.g., the left panels in Figures 5 and 6), the first mode contains clockwise orbits around Sgr A* while the second mode contains counterclockwise orbits around Sgr A*. The clockwise orbits follow the general direction of gas flow in the CMZ and are henceforth

 $[\]overline{11}$ The positional uncertainty of ${\sim}10$ mas for Sgr A* is negligible in this analysis and is ignored.

 $^{^{12}}$ The proper-motion uncertainty of $\sim\!\!0.008$ mas yr^{-1} for Sgr A^* is negligible in this analysis and is ignored.

Mode 1 Probability: 0.5

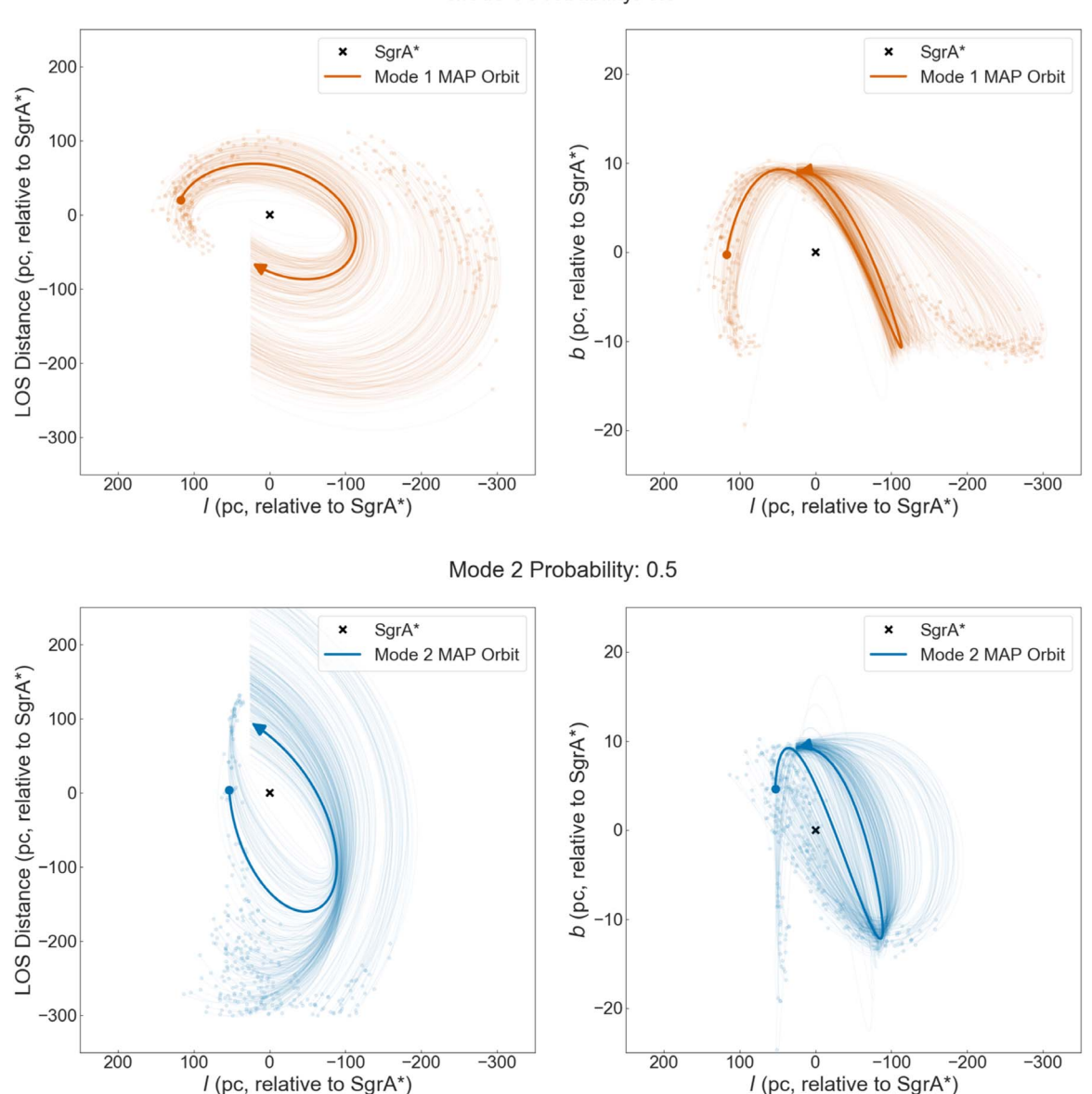


Figure 5. Orbits drawn from the two solution modes for the Arches cluster. Each row represents a different mode, with the left panel showing a "top-down" view of the orbits from the North Galactic Pole (with Earth at negative LOS distance) and the right panel showing an "edge-on" view of the orbits from the Galactic Plane. The maximum a posteriori (MAP) orbit for each mode is represented by the thick line, with a distribution of orbits drawn from the posterior shown by the thin lines. On the MAP orbit, the arrowhead shows the current position of the cluster while the circle shows the birth location of the cluster. On the sample of orbits drawn from the posterior, the birth locations of the individual orbits are represented by the smaller and fainter circles. The overall probability of each mode is given in the title of each row

referred to as prograde orbits. The counterclockwise orbits move in the opposite direction and are thus referred to as retrograde orbits. A summary of each mode, including the parameters for the maximum a posteriori (MAP) orbit, is provided in Table 8. The full posterior probability distributions for the free parameters of θ are presented in Appendix C.

The range of allowed orbits is primarily driven by the uncertainty in the present-day line-of-sight distance to the cluster, $d_{\rm los}$. As found in previous work (Stolte et al. 2008, 2014; Libralato et al. 2020), prograde orbits place the clusters in front of Sgr A* relative to Earth (negative $d_{\rm los}$) while retrograde orbits place the clusters behind Sgr A* (positive $d_{\rm los}$). Figure 7 shows four orbit metrics as a function of $d_{\rm los}$: the periapse distance, the ratio of apoapse to periapse

distance, the radial period (i.e., the time it takes for the cluster to travel from apoapse to periapse and back; Binney & Tremaine 2008), and ratio of cluster age to radial period. While the total range of values for these metrics is large, they are reasonably well constrained for a given d_{los} .

It is important to note that although $d_{\rm los}$ is not constrained by our likelihood function (other than the requirement that $|d_{\rm los}| < 300\,{\rm pc}$), it does not mean that each value of $d_{\rm los}$ is equally likely in the orbit posteriors. The probability distributions of $d_{\rm los}$ for the clusters is shown in Figure 8. While broad, the $d_{\rm los}$ distributions are not uniform because the other kinematic parameters of the clusters (three-dimensional velocity, two-dimensional sky position) are constrained by observations. Thus, the volume of parameter space (initial

Mode 1 Probability: 0.61

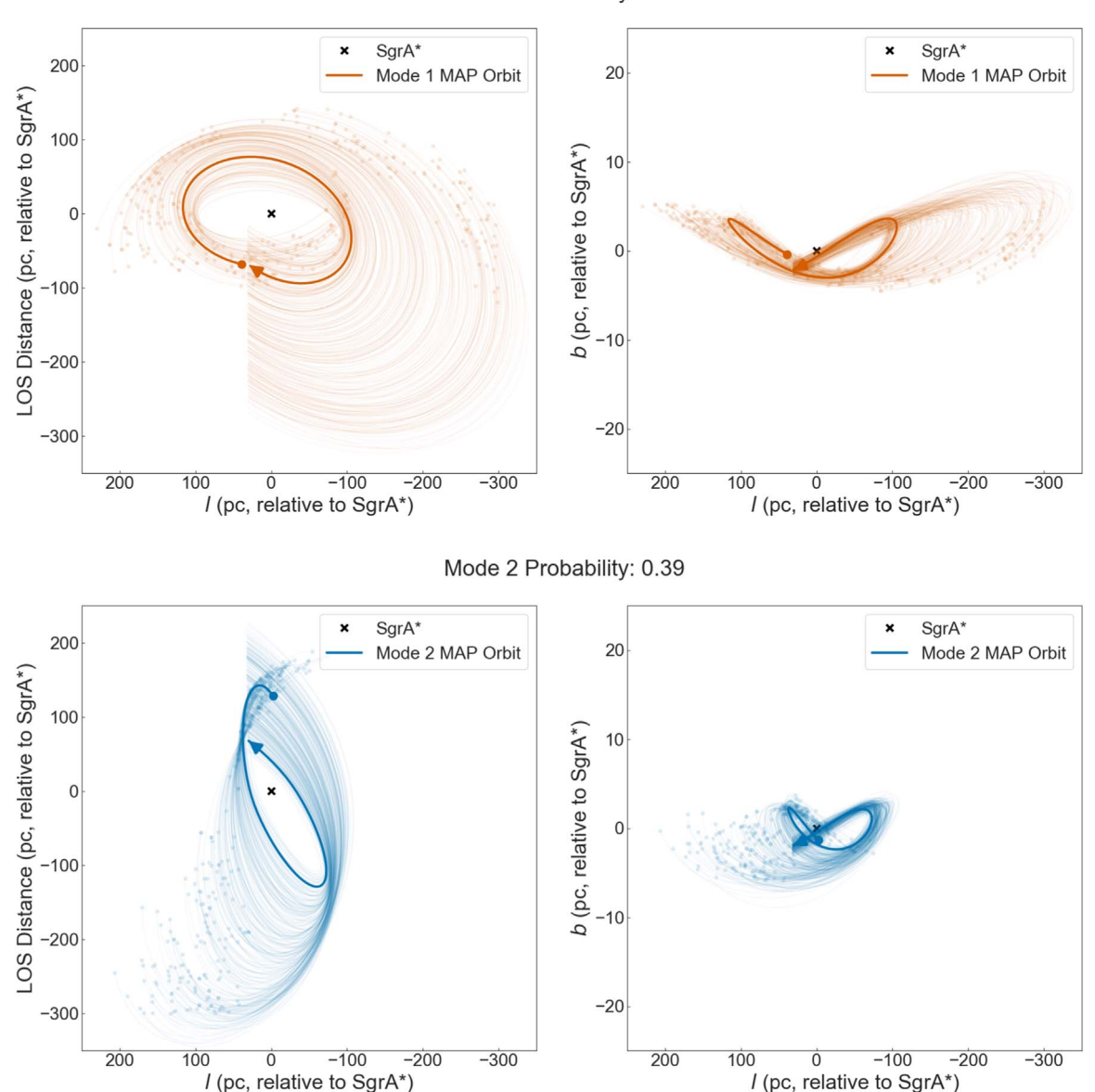


Figure 6. Orbits drawn from the two solution modes for the Quintuplet cluster, plotted in same manner as Figure 5.

Table 8
Summary of Cluster Orbit Solution Modes

						Maximum a Posteriori Parameters							
Cluster	Mode	Direction	log-evidence	Prob	x_b pc	у _ь рс	z_b pc	$km s^{-1}$	$\frac{vy_b}{\text{km s}^{-1}}$	$km s^{-1}$	$t_{\rm clust}$ $\log({ m years})$		
Arches	1	Prograde	-64.10	0.50	-20.3	117.4	-0.3	-106.8	-46.7	23.7	6.47		
Arches	2	Retrograde	-64.10	0.50	-4.1	53.2	4.6	249.3	-15.3	26.2	6.49		
Quintuplet	1	Prograde	-63.72	0.61	68.0	39.3	-0.4	-41.2	181.8	9.2	6.59		
Quintuplet	2	Retrograde	-64.15	0.39	-128.1	-2.3	-1.3	-82.2	50.8	4.1	6.60		

Note. Description of columns. Mode: number of mode. Direction: the direction of the orbits relative to the general gas flow observed in the CMZ. log-evidence: ln(P(d)), as defined in Equation (4). Prob: the probability of the solution mode, x_b , y_b , z_b , vx_b , vy_b , and vz_b . t_{clust} : parameters of MAP orbit within the mode, in the same coordinate system as Table 6.

position and velocity) that can produce suitable orbits with a similar value of $d_{\rm los}$ is not necessarily equal. In addition, there are cases where the initial conditions required to obtain an orbit with a given $d_{\rm los}$ fall outside the boundaries of our priors (i.e.,

they are not consistent with our assumption that the clusters formed within the CMZ) and are not allowed by our model.

The ratio of the probability of a given mode to the probability of the most likely mode can be calculated from

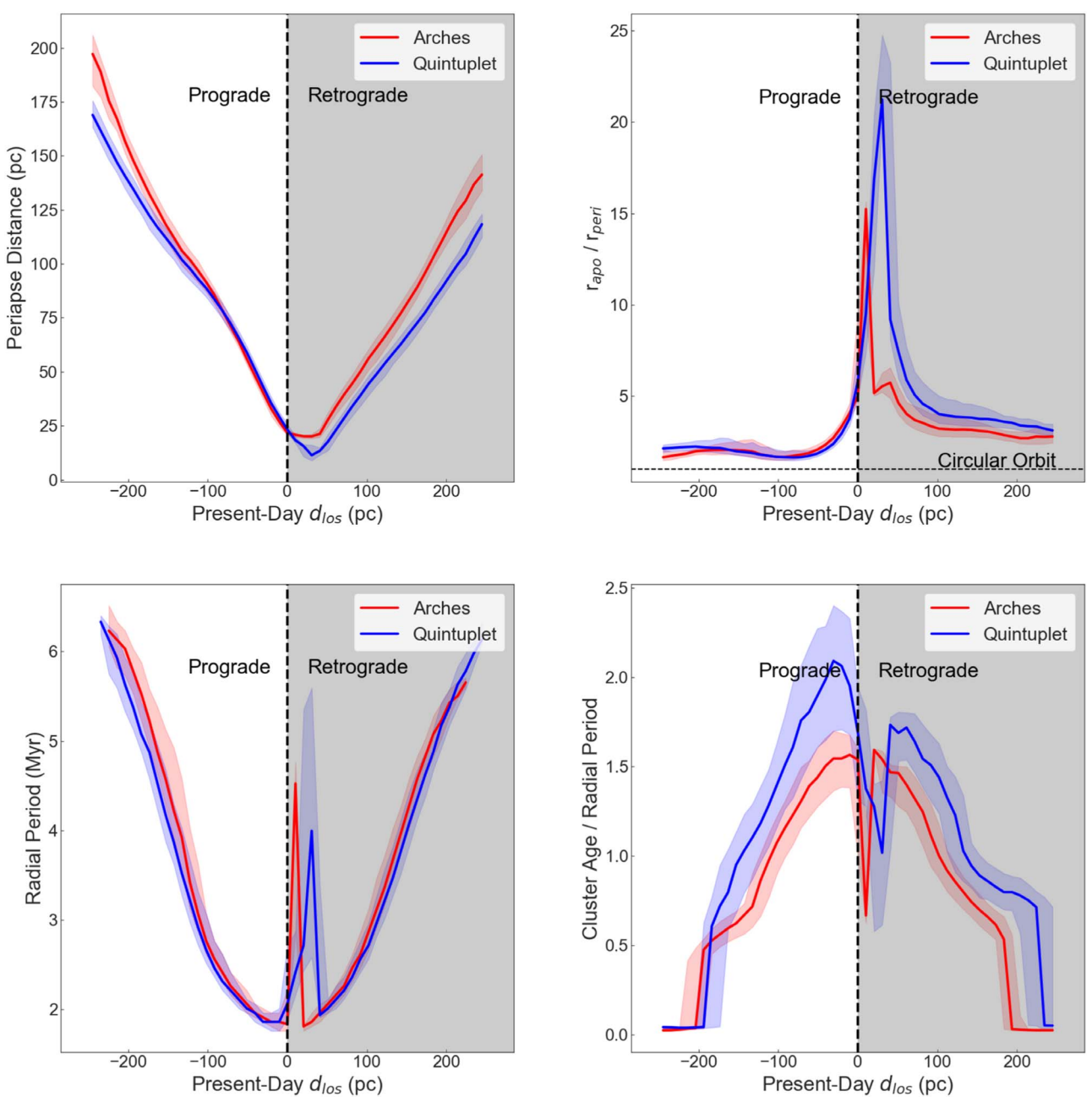


Figure 7. Periapse distance (top left), ratio of apoapse to periapse (top right), radial period (bottom left), and ratio of cluster age to radial period (bottom right) as a function of d_{los} for the Arches (red) and Quintuplet (blue) clusters. For each cluster, the solid line represents the 50th percentile in each radius bin, while the shaded region represents the range between the 15.9th and 84.1th percentiles (1σ) in that bin. The black dotted line separates the prograde orbits from the retrograde orbits. For the remainder of the paper, only the prograde orbits are considered.

the Bayes factor:

$$\psi_i = \frac{P(\mathbf{x})_i}{P(\mathbf{x})_{\text{max}}},\tag{7}$$

where $P(x)_i$ is the evidence of the *i*th mode and $P(x)_{max}$ is the evidence of the most likely mode (i.e., the mode with the largest evidence). The mode probabilities are calculated by renormalizing these ratios across all modes to sum to 1:

$$Prob_i = \frac{\psi_i}{\sum_j^m \psi_j},\tag{8}$$

where m is the total number of modes for the cluster. The probabilities for the modes are reported in the plot titles of

Figures 5 and 6 as well as in Table 8. For the Arches cluster, the prograde and retrograde solution modes have equal probability, while for the Quintuplet cluster the prograde mode is slightly favored. The asymmetry in the Quintuplet mode probabilities is largely because more retrograde orbits are disallowed by the prior boundaries compared to the prograde orbits.

While both prograde and retrograde orbit solutions are allowed by this analysis, it is unclear how the clusters could have formed on retrograde orbits. This would imply that their natal molecular clouds, which must have been quite massive in order to create the clusters, must also have been on retrograde orbits. Such high-mass retrograde clouds have not been found in observations or simulations. As a result, we restrict the

remaining analysis in the paper to the prograde solution mode only. When statistical quantities are calculated, such as 3σ limits or probability contours, the probability of the retrograde mode is set to zero and only the prograde mode is considered.

6.1. Orbit Properties

We integrate the orbits from the model posteriors forward 10 Myr in order to place statistical constraints on several properties of interest. The probability distributions for the closest approach of each cluster to Sgr A* are shown in the left panel of Figure 9. The closest approach distance is directly related to $d_{\rm los}$; the smaller the value for $d_{\rm los}$, the closer the cluster approaches Sgr A*. We place 3σ lower limits of 24.7 pc and 29.8 pc for the closest approach of the Arches and Quintuplet, respectively. This raises the question of whether dynamical friction, which is ignored in these orbit calculations, could cause either cluster to spiral inward and merge with either the NSC or young nuclear cluster (YNC) before being tidally disrupted. This is discussed further in Section 7.3.

The ratio of the apoapse to periapse distance $(r_{\rm apo}/r_{\rm peri})$ provides a measure of the eccentricity of the orbits. The clusters share a similar probability distribution for this ratio, with a 50th percentile of \sim 1.9 (equivalent to an eccentricity of \sim 0.31) and a tail that extends to larger values (Figure 9, right panel). The distributions have 3σ lower limits of $r_{\rm apo}/r_{\rm peri}\sim$ 1.4, indicating that neither cluster can be on a circular orbit, in agreement with past studies (Stolte et al. 2008, 2014; Libralato et al. 2020). The largest values of $r_{\rm apo}/r_{\rm peri}$ occur as $d_{\rm los}$ decreases. The radial period of the clusters also depends on $d_{\rm los}$, ranging

The radial period of the clusters also depends on $d_{\rm los}$, ranging from $\sim\!2$ Myr for small $d_{\rm los}$ to $\sim\!6$ Myr for large $d_{\rm los}$ (Figure 7, lower-left panel). The Arches cluster has completed at least one complete radial period if $d_{\rm los}\lesssim 100$ pc while the Quintuplet has completed at least one radial period if $d_{\rm los}\lesssim 140$ pc (Figure 7, lower-right panel).

6.2. The Clusters Do Not Share a Common Orbit

Whether the Arches and Quintuplet clusters share a common orbit has significant implications for their formation mechanism. Our results reveal that the cluster orbits appear to be similar in the the "top-down" view (left panels of Figures 5 and 6), as has been noted in past work (e.g., Stolte et al. 2014; Libralato et al. 2020). This suggests that the clusters likely share a similar formation mechanism. However, the "edge-on" view of the orbits reveals that the Arches tends to exhibit larger vertical oscillations in the Galactic Plane compared to the Quintuplet (right panels of Figures 5 and 6). This difference is more clearly seen in a comparison of the probability distributions for the maximum deviation of the orbit from the Galactic Plane, which we define as $b_{\rm max}$ (Figure 10, left panel).

The probability that b_{max} is consistent between the Arches and Quintuplet, $P(b_{\text{max,arch}=\text{quint}})$, can be calculated as

$$P(b_{\rm max,arch=quint}) = \int_{-\infty}^{\infty} P_{\rm arch}(b_{\rm max}) P_{\rm quint}(b_{\rm max}) db_{\rm max}, \quad (9)$$

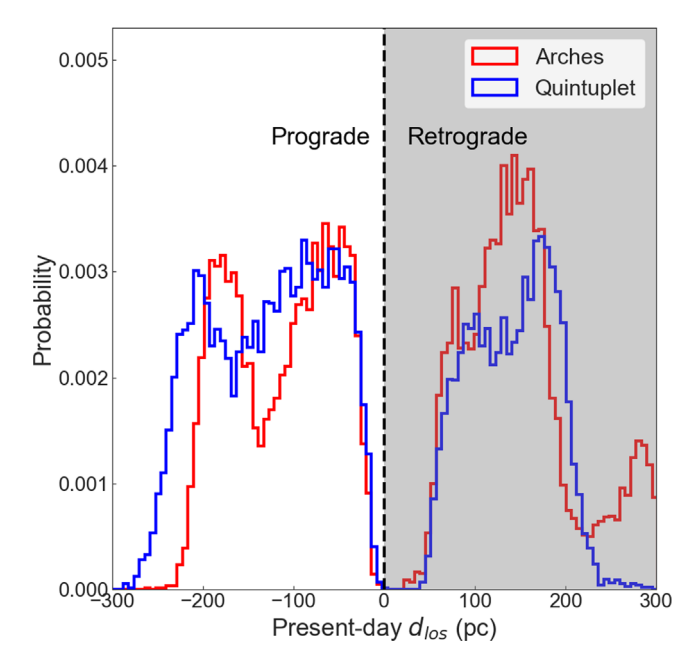


Figure 8. Probability distributions for the present-day $d_{\rm los}$ of the Arches (red) and Quintuplet (blue) clusters calculated from the orbit model posteriors. Although $d_{\rm los}$ is not constrained by Equations (5) and (6), these distributions are not uniform because the other kinematic parameters of the clusters (three-dimensional velocity, two-dimensional sky position) are constrained by observations. In addition, the boundaries on the model priors (set by the assumption that the clusters formed within the CMZ; see Section 5.1) disfavor certain values of $d_{\rm los}$.

where $P_{\rm arch}(b_{\rm max})$ and $P_{\rm quint}(b_{\rm max})$ are the probability distributions of $b_{\rm max}$ for the Arches and Quintuplet, respectively. We find that $P(b_{\rm max,arch=quint})=0.01\%$, which corresponds to a difference of $\sim 3.9\sigma$. We therefore conclude that the $b_{\rm max}$ distributions of the clusters are inconsistent.

The difference between the cluster orbits is also reflected in their birth properties, in particular the joint probability distribution of birth v_b versus birth b (Figure 10, right panel). While the one-dimensional distributions of these properties have significant overlap (e.g., if one were to examine either birth b or birth v_b alone and marginalize over the other dimension), they distinctly separate in two-dimensional space. For a given value of b, the distribution of birth v_b for the Arches has significantly higher absolute values than the same distribution for the Quintuplet.

Thus, we conclude that the clusters cannot share a common orbit. The difference in their orbits can be traced to the difference between their present-day b positions ($\Delta b = 0.0789 \pm 0.008$), which corresponds to a difference of ~ 11 pc at the distance of the GC. We will discuss the implications of this result in the context of possible cluster formation scenarios in Section 7.2.

7. Discussion

In this section, we compare our measurements of the absolute proper motion of the Arches and Quintuplet clusters to past work (Section 7.1) and place our constraints on the cluster orbits in the context of proposed formation scenarios (Section 7.2). We also discuss whether the clusters are likely to inspiral into the NSC within their lifetimes (Section 7.3) and explore the impact that our assumptions about the GC gravitational potential have on the orbit results (Section 7.4).

 $[\]overline{^{13}}$ Figure 7 also reveals a sharp increase in $r_{\rm apo}/r_{\rm peri}$ for small positive values of $d_{\rm los}$. This is caused by highly eccentric retrograde orbits that become possible if the clusters formed nearly 300 pc from Sgr A* (the edge of the birth location prior). While such orbits could bring the clusters as close as ~ 15 pc to Sgr A*, it would not be close enough to cause a merger with the NSC (Section 7.3). As discussed in the text, we do not investigate the retrograde orbits in further detail.

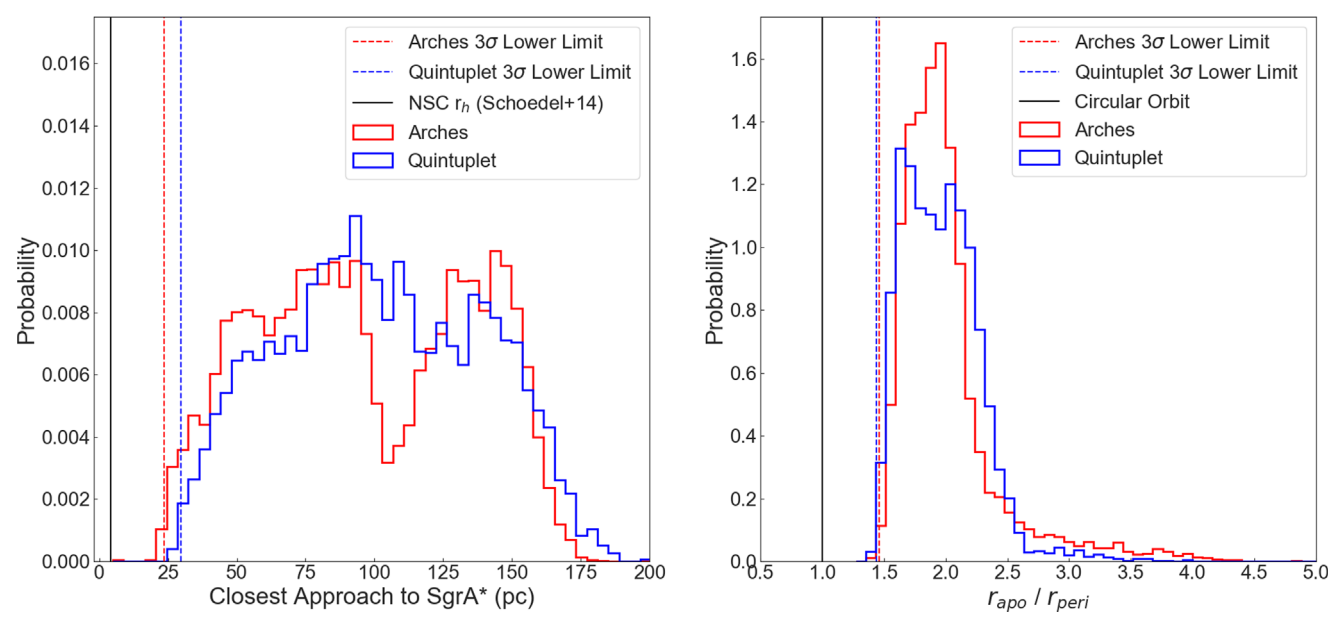


Figure 9. Left: the probability distributions for the closest approach to Sgr A* for the Arches (red histogram) and Quintuplet (blue histogram) orbits, compared to the half-light radius of the NSC (black line, 4.2 pc; Schödel et al. 2014). We obtain 3σ limits of 24.7 pc for the closest approach of the Arches (red dotted line) and 29.8 pc for the closest approach of the Quintuplet (blue dotted line). Right: the probability distributions for $r_{\rm apo}/r_{\rm peri}$, which gives a measure of the orbit eccentricity. Neither cluster is consistent with a circular orbit ($r_{\rm apo}/r_{\rm peri} = 1.0$, black line); the 3σ lower limit is \sim 1.4 for both clusters (blue and red dotted lines). The 50th percentile value for $r_{\rm apo}/r_{\rm peri} \sim 1.9$ for both clusters, which is approximately equal to an eccentricity of \sim 0.31. Note that only the prograde orbit modes are considered in these plots.

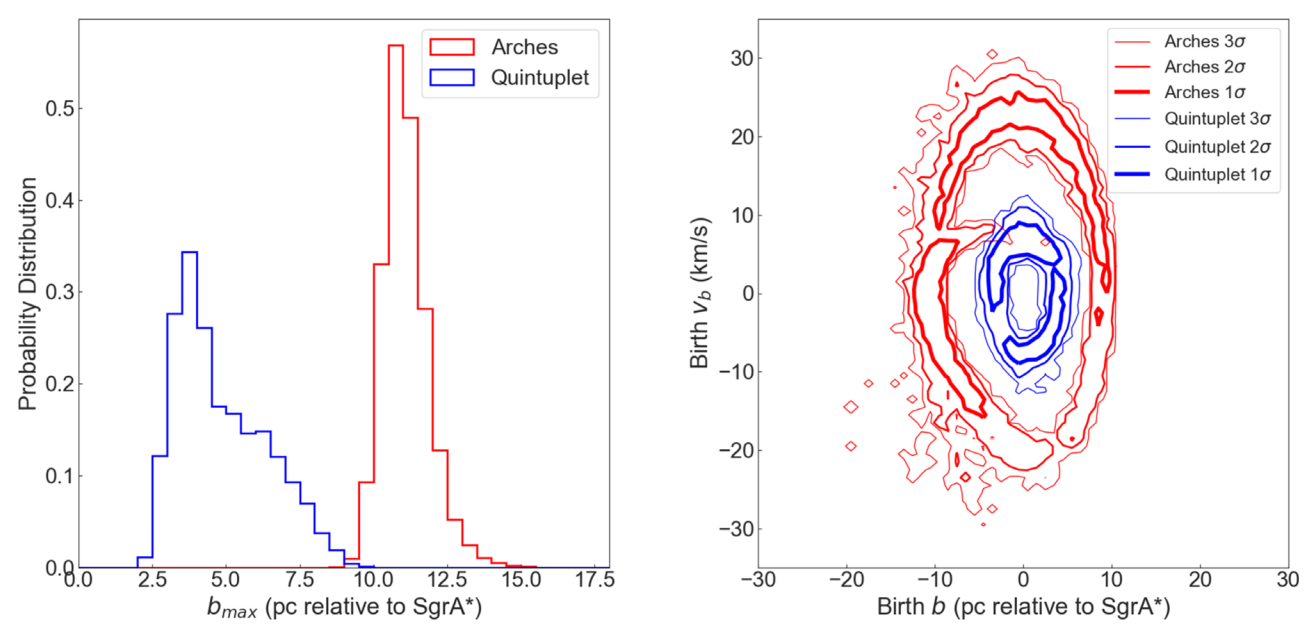


Figure 10. A comparison of the orbital properties of the Arches (red) and Quintuplet (blue) clusters that are associated with the vertical oscillations of their orbits in the Galactic Plane. Left: the probability distributions for the maximum vertical deviation of the orbits from the Galactic Plane (b_{max}). The distributions are discrepant by $\sim 3.9\sigma$ and are thus inconsistent. Right: the joint probability distributions of the birth v_b versus birth b for the clusters. For a given b, the Arches formed with a significantly larger birth v_b (in terms of absolute value) than the Quintuplet. Note that only the prograde orbit modes are considered in these plots.

7.1. Arches and Quintuplet Absolute Motion: Comparison to Literature

We present the most precise measurements of the absolute proper motions of the Arches and Quintuplet clusters made to date. A comparison between our measurements and those in the literature is shown in Figure 11. Note that we convert all proper-motion measurements into Galactic coordinates (μ_{l^*} , μ_b) relative to Sgr A* (e.g., the Sgr A*-at-Rest reference frame) for this comparison.

Stolte et al. (2008), Clarkson et al. (2012), and Stolte et al. (2014) measure the relative proper motion of the clusters with respect to the field star population and assume that this is equivalent to the motion of the clusters in the Sgr A*-at-Rest reference frame. To convert to Galactic coordinates, we rotate their measurements and corresponding uncertainties to the position angle of the Galactic Plane (31°.40). Although our measurements are somewhat different than these past studies (for example, our value for μ_{l*} is generally smaller for the

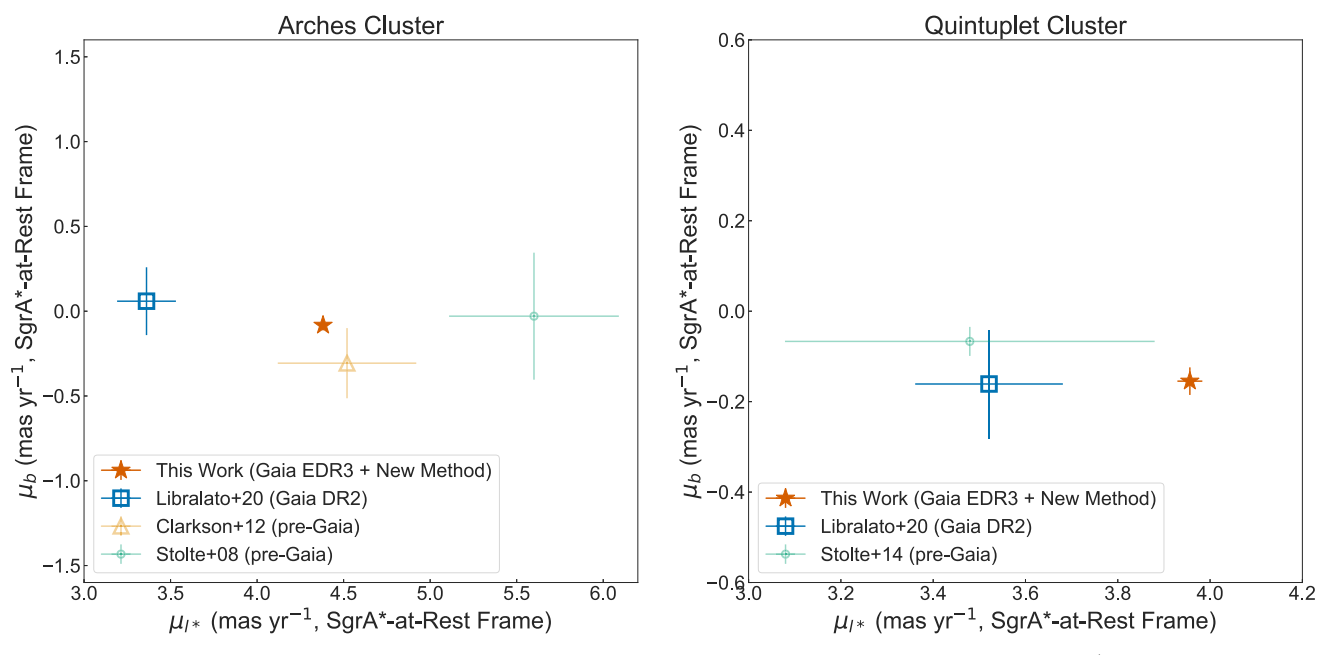


Figure 11. Proper-motion measurements of the Arches (left) and Quintuplet (right) clusters in Galactic coordinates in the Sgr A*-at-Rest reference frame. The measurements from this work (red filled stars) and Libralato et al. (2020, open blue squares) are derived using Gaia. Pre-Gaia measurements by Stolte et al. (2008), Clarkson et al. (2012), and Stolte et al. (2014) (open circles and triangles) are derived from the relative proper motion between the clusters and field stars. We make the most precise measurement of the absolute proper motions of the clusters to date.

Arches and generally larger for the Quintuplet), they are consistent to within 3σ of the combined uncertainty. However, our measurements are significantly more precise, with $\gtrsim \! 10 \times \!$ smaller uncertainties than these past measurements. In addition, it is unclear whether the assumption that the relative proper motion of the clusters is equivalent to their motion in the Sgr A*-at-Rest reference frame is valid. This requires that the average field star motion is at rest relative to Sgr A*—in other words, that the observations are deep enough such that the streaming motion of the field stars in front of Sgr A* cancels out with the streaming motion of the field stars behind Sgr A*. Further, the field star population has been shown to exhibit multiple kinematic substructures, making it challenging to interpret the average field star proper motion (Hosek et al. 2015; Rui et al. 2019).

Similar to this work, Libralato et al. (2020) measure the absolute proper motion of the clusters in the Gaia reference frame. In the same manner as our measurements, we subtract the absolute motion of Sgr A* (Reid & Brunthaler 2020) to get the cluster motions in the Sgr A*-at-Rest reference frame. For the Arches, our value for μ_{l*} is significantly larger (4.38 \pm 0.026 mas yr $^{-1}$ versus 3.36 \pm 0.17 mas yr $^{-1}$), which represents a 6σ difference in terms of the combined uncertainty. All other measurements agree within 3σ .

Our proper-motion uncertainties are $\sim 5\times$ smaller than those of Libralato et al. (2020), which can be explained by differences in our data and methodology. Briefly, Libralato et al. (2020) identify a set of stars in the Gaia DR2 catalog that are also found in the published proper-motion catalogs of the clusters from Stolte et al. (2015). They find 4 suitable matches in the Arches field and 12 suitable matches in the Quintuplet field. They then calculate the error-weighted difference between the Gaia proper motions and the Stolte et al. (2015) proper

motions for these stars. Since the Stolte et al. (2015) catalog is constructed in a reference frame where the cluster is at rest, the average difference between the Gaia and Stolte et al. (2015) proper motions is interpreted to be the difference between the cluster-at-rest and Gaia reference frames and thus represents the absolute proper motions of the clusters.

Our data and methodology offer several improvements to this approach. First, the HST WFC3-IR data provides a larger field of view of the clusters and thus contains significantly more Gaia stars (26 reference stars for the Arches field and 28 reference stars for the Quintuplet field; Section 3.1). As a result, we transform the HST astrometry into the Gaia reference frame with higher precision and accuracy. The fact that Libralato et al. (2020) were limited to only four Gaia reference stars for the Arches cluster likely explains the sizable discrepancy with our proper-motion measurements. Second, we convert the HST astrometry into the Gaia reference frame on an epoch-by-epoch basis, using spatially dependent transformations to correct for optical distortions and other biases. This allows us to measure proper motions in the Gaia frame directly, explore the quality of the proper-motion fits and corresponding uncertainties, and search for remaining distortions or systematics in the astrometry (Section 3.3 and Appendix A). Third, the Gaia EDR3 catalog offers improved position and proper-motion measurements compared to DR2. These improvements include the use of more data (34 months versus 22 months of observations) and the introduction of color-dependent correction terms to reduce astrometric biases. As a result, the position and proper-motion uncertainties in the EDR3 catalog are generally improved by a factor of ~ 0.8 and ~ 0.5 compared to DR2, respectively (Lindegren et al. 2021).

7.2. Comparing Possible Formation Scenarios for the Clusters

We evaluate our results in the context of two proposed formation scenarios for the Arches and Quintuplet clusters: the x_1 – x_2 collision scenario, in which the clusters formed in

¹⁴ Stolte et al. (2015) derive proper motions using ground-based adaptive optics observations of the clusters using the NAOS-CONICA system on the VLT (Rousset et al. 2003; Lenzen et al. 2003) made over a 3–5 yr baseline.

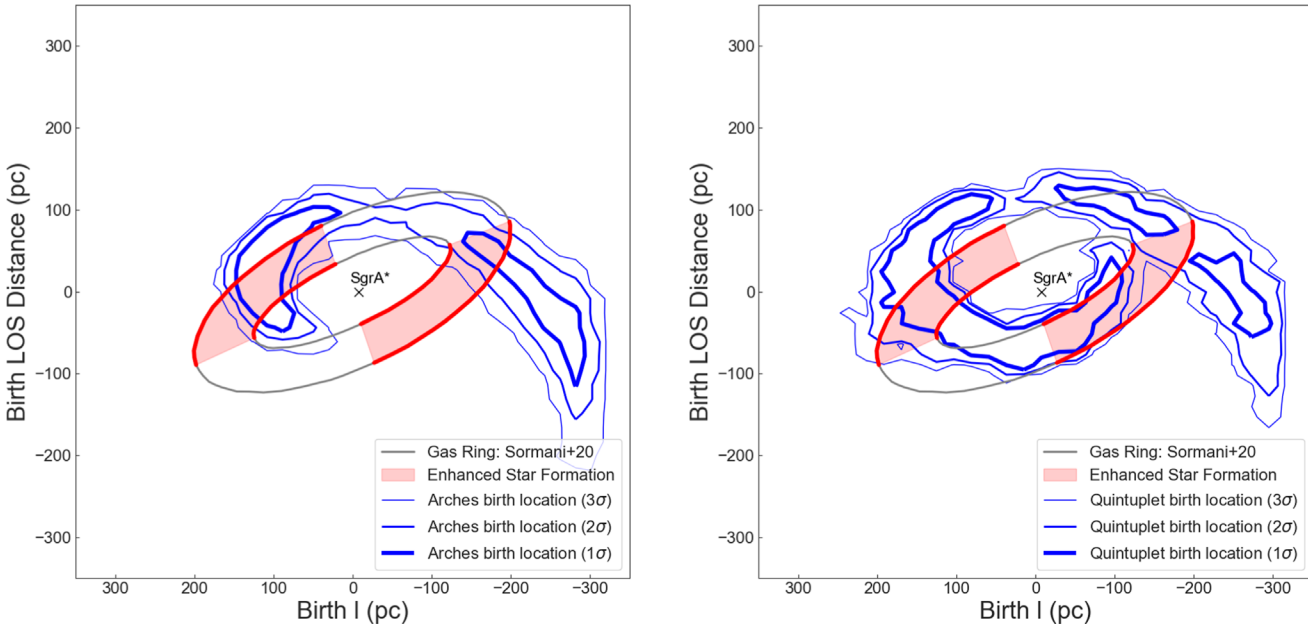


Figure 12. Constraints on the cluster birth location (blue contours, representing 1σ , 2σ , and 3σ contours with lines of decreasing thickness) for the Arches (left) and Quintuplet (right) clusters, compared to the dense CMZ gas ring predicted by simulations (gray ring; Sormani et al. 2020b). In the x_1-x_2 gas collision scenario, enhanced star formation activity is expected between the apoapse and following periapse of the gas ring (red shaded regions). We find that both clusters are consistent with forming in these areas of enhanced formation, although the uncertainties are large. The cluster constraints are for the prograde solution mode only.

collisions between gas on x_1 and x_2 orbits, and the open stream scenario, where the clusters formed from the collapse of molecular clouds on the proposed KDL15 orbit. Both scenarios would place the clusters on prograde orbits and so only the prograde solution modes are considered in this analysis. We also consider whether the clusters could have formed within the dust lanes before the x_1 – x_2 collision region, another location where star formation might occur (e.g., Sormani et al. 2020b).

7.2.1. The x_1-x_2 Collision Scenario

The regions where gas from x_1 orbits intersect with gas on x_2 orbits have long been identified as locations where gas will shock and compress (e.g., Binney et al. 1991; Morris & Serabyn 1996). It is often suggested that these collisions trigger local enhancements in star formation activity, which has been invoked to explain ring-like structures of star formation commonly found in the nuclei of spiral galaxies (e.g., Böker et al. 2008). Recent hydrodynamic simulations of the CMZ predict that a ring of dense gas forms along the x_2 orbits with a radius of \sim 100–200 pc, and that collisions with infalling x_1 gas occur near the apoapse of this ring (Tress et al. 2020). These collisions produce dense molecular clouds that grow progressively more massive and compact due to self-gravity. Star formation can occur throughout the gas ring, but peaks in the area between the apoapse and following periapse of the ring (Sormani et al. 2020b).

Stolte et al. (2008, 2014) argue that this is a viable formation scenario for the Arches and Quintuplet clusters because (1) the birth locations they derive for the clusters are consistent with the apoapse of the x_2 orbits where these collisions occur, and (2) their measurements of the present-day three-dimensional velocities of the clusters (172 \pm 15 km s⁻¹ and 167 \pm 15 km s⁻¹ relative to Sgr A* for the Arches and Quintuplet, respectively) are significantly higher than the maximum expected velocity of gas on x_2 orbits (120 km s⁻¹; Englmaier & Gerhard 1999). They suggest that this could be the result of a gas collision

where the clusters gained momentum from the higher-velocity infalling x_1 cloud. We re-examine these arguments in light of our updated constraints on the birth locations and velocities of the clusters.

In Figure 12, we compare our constraints on the birth location of the Arches and Quintuplet clusters to the CMZ gas ring predicted by Sormani et al. (2020b). We find that the highest-probability contours for the birth location of the Arches generally fall between apoapse and the following periapse of the ring, consistent with the expected region of enhanced star formation in the x_1 – x_2 collision scenario. The birth location of the Quintuplet is also generally consistent with the x_1 – x_2 collision scenario, although the constraints are weaker. Unlike the Arches, there is a significant probability that the Quintuplet formed at nearly any point throughout the gas ring. This is likely because the Quintuplet is older and has a larger uncertainty on its age (Table 6), and so its birth location is less constrained.

In Figure 13, we compare our constraints on the birth $v_{\rm los}$ of the clusters to the predicted envelope of $v_{\rm los}$ values for gas on x_2 orbits from Englmaier & Gerhard (1999). We obtain a similar result for both clusters: For birth locations that are consistent with the gas ring ($|l| \lesssim 200\,{\rm pc}$), the birth $v_{\rm los}$ for the clusters appear to be fully consistent with the x_2 orbits, with no evidence of velocity enhancement. Only when the cluster birth locations are outside the gas ring ($l \lesssim -200\,{\rm pc}$) is there

The shape of the gas ring is taken from Figure 12 of Sormani et al. (2020b). Note that in their figure, the *x*-axis is oriented along the major axis of the bar such that the Sun is located in the positive *x* direction with an Earth–GC-bar angle of 20° (Sormani et al. 2018). In our Figure 12, the axes are oriented such that Earth is located at (0, 8.09) kpc. Thus, we rotate the Sormani et al. (2020b) gas ring clockwise by $90^{\circ} + 20^{\circ} = 110^{\circ}$. While this structure will gradually rotate with time due to the pattern speed of the bar, we note that it would have only rotated by $\sim 12^{\circ} - 18^{\circ}$ at most since the time the cluster formed, assuming a cluster age of ~ 5 Myr and a bar pattern speed of 40-63 km s⁻¹ kpc⁻¹ (Bland-Hawthorn & Gerhard 2016). This additional rotation is insignificant compared to the uncertainties in the cluster birth location constraints and thus is ignored.

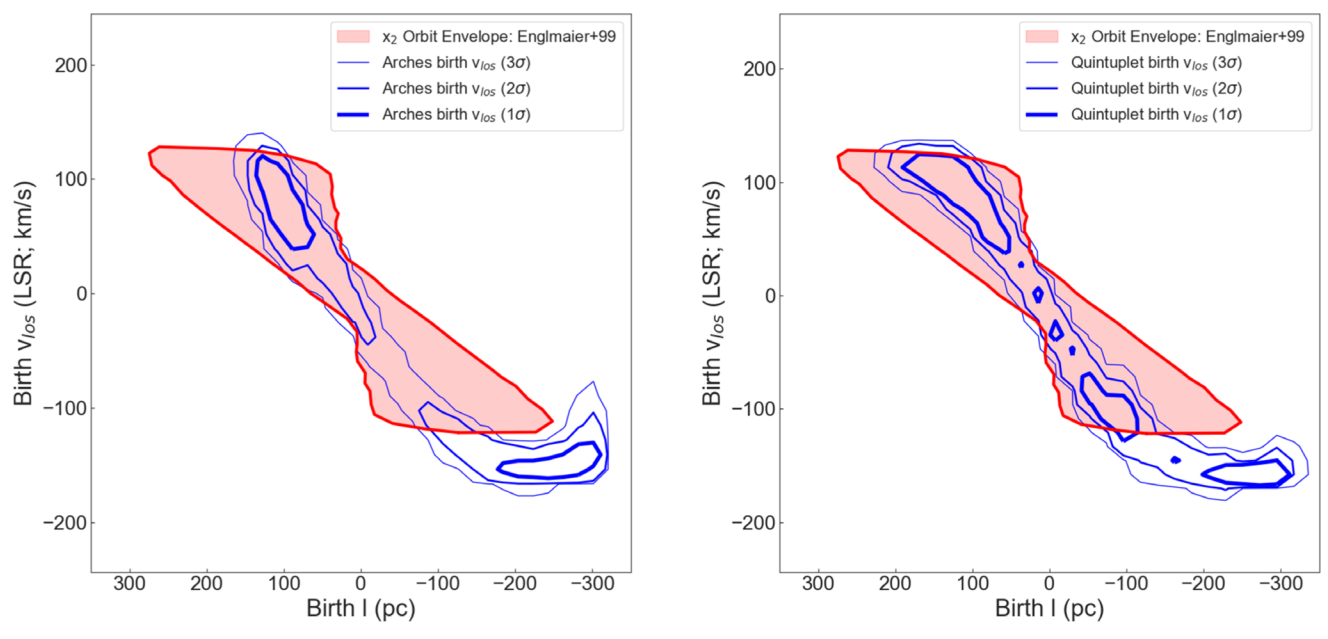


Figure 13. Constraints on the birth v_{los} vs. birth l (blue contours, representing 1σ , 2σ , and 3σ contours with lines of decreasing thickness) for the Arches (left) and Quintuplet (right) clusters, compared to the envelope of expected v_{los} values for gas on x_2 orbits (red shaded region; Englmaier & Gerhard 1999). For both clusters, the birth v_{los} values are consistent with the x_2 envelope where the birth locations of the clusters are consistent with forming in the dense gas ring in the first place ($|l| \lesssim 200$ pc). The cluster constraints are for the prograde solution mode only.

evidence of an enhanced birth $v_{\rm los}$ at 3σ significance. However, the clusters would no longer be consistent with the x_1 - x_2 collisions at these radii, and so we do not interpret this as evidence in favor of this scenario.

We conclude that our results offer mild support for the x_1 – x_2 collision scenario. The birth locations of the clusters appear consistent with the expected regions of enhanced star formation, although the uncertainty in the constraints is admittedly large. We do not find evidence for an enhancement in the birth v_{los} of the clusters relative to the x_2 orbits at birth locations where the clusters are consistent with forming within the dense gas ring. However, it is not yet clear how large of a velocity enhancement might be expected from a gas collision and whether or not it could be observed. Stolte et al. (2008) point out that the degree to which the cluster's birth velocity is enhanced would depend on many factors including the geometry of the collision and the relative densities of the clouds involved; additional theoretical work is needed to explore these effects. Finally, we do not consider the fact that the Arches and Quintuplet clusters have different orbits to be a challenge to the x_1-x_2 collision scenario. It would be no surprise that two clusters that formed via gas collisions at different times in the tumultuous CMZ would have sufficiently different initial conditions in b and v_b to account for the difference in the vertical oscillations seen in their orbits.

7.2.2. The Open Stream Scenario

If the clusters formed via the open stream scenario, then we would expect their present-day positions and motions to be consistent with the KDL15 orbit as it is unlikely that the clusters could have significantly deviated from their natal orbit by their current age (\lesssim 5 Myr). Due to the uncertainty in $d_{\rm los}$, there are three possible locations for the Arches and Quintuplet clusters on the KDL15 orbit (Figure 14). At each of these intersection points, we calculate the probability of obtaining the observed properties $x_{\rm int} = \{b, \mu_{l*}, \mu_b, v_{\rm los}\}$ of the clusters under

the assumption that they are on the proposed orbit. Note that x_{int} does not include the l or d_{los} ; this is because the intersection points are defined such that l and d_{los} match the values on the orbit. We define x_{int} using the values in Table 7.

For each dimension of x_{int} , the probability of obtaining the observed value $(x_{int,i})$ given the predicted value on the KDL15 orbit $(x_{kdl,i})$ is

$$P(x_{\text{int},i}) = \frac{1}{\sigma_{\text{tot}}\sqrt{2\pi}} e^{-\frac{1}{2} \left(\frac{x_{\text{int},i} - x_{kdl,i}}{\sigma_{\text{tot}}}\right)^2},$$
(10)

where $\sigma_{\rm tot}^2 = \sigma_{x_{\rm int,i}}^2 + \sigma_{x_{kdl,i}}^2$, and $\sigma_{x_{\rm int,i}}$ and $\sigma_{x_{kdl,i}}$ are the uncertainties in the observed data and KDL15 orbit value. ¹⁶ The probability over all dimensions is then

$$P(\mathbf{x}_{\text{int}}) = \prod_{i} P(\mathbf{x}_{\text{int},i}). \tag{11}$$

Table 9 shows the values of $P(x_{\rm int})$ at the intersection points for both clusters. Both clusters are inconsistent with the stream 2 and stream 3 intersection points, which are discrepant with observations by 4σ – 5σ and $>10\sigma$, respectively (Appendix D.2). However, we find that the clusters are marginally consistent with the stream 1 intersection point at the 2.71 σ and 2.57 σ level for the Arches and Quintuplet, respectively (Figure 15). Note that the uncertainty in this comparison is almost entirely due to the KDL15 orbit model rather than the cluster measurements themselves.

Although the clusters are individually consistent with the KDL15 orbit within the considerable uncertainties, a challenge for the open stream scenario is that the clusters do not share a common orbit (Section 6.2). Thus, the difference between the vertical oscillations of the cluster orbits would need to be explained by intrinsic latitudinal differences between individual molecular clouds on the open stream. However, it is unclear if this is possible while maintaining the

The We calculate $\sigma_{x_{kdl,i}}$ via a Monte Carlo simulation over the best-fit orbit parameters from KDL15 as described in Appendix D.1.

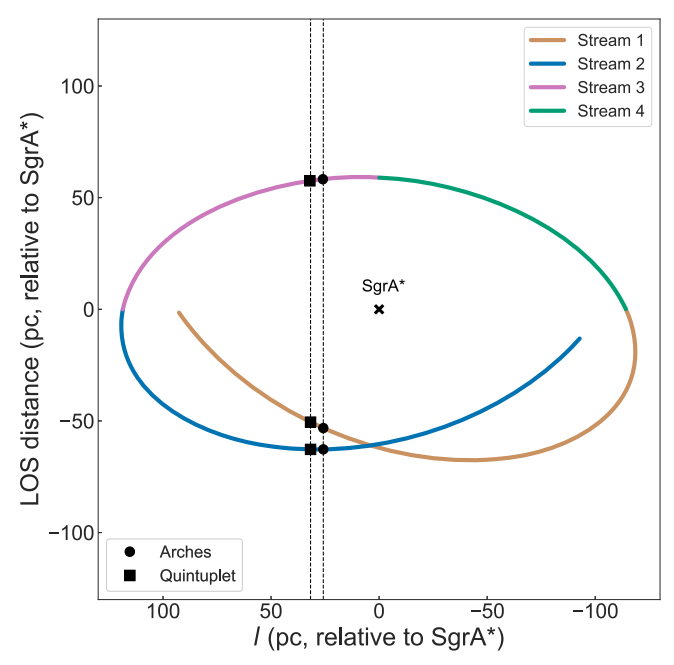


Figure 14. Proposed KDL15 orbit, plotted as the line-of-sight distance from Sgr A* versus galactic longitude *l*. The points at which the Arches and Quintuplet clusters intersect the orbit are marked by circles and squares, respectively. Using the nomenclature from KDL15, these intersections occur on streams 1, 2, and 3 (different color line segments).

Table 9
Probability of Obtaining the Observed Measurements at the KDL15 Orbit
Intersection Points

	Arches (Cluster	Quintuplet Cluster			
Stream	log(Prob)	Sigma	log(Prob)	Sigma		
1	-5.00	2.71	-4.58	2.57		
2	-10.74	4.25	-14.07	4.94		
3	-95.63	>10	-65.23	>10		

Note. Description of columns. Stream = KDL15 orbit stream. log (Prob) = Natural log of the probability described in Equation (11). Sigma = the probability from Equation (11) converted into σ , assuming Gaussian statistics.

overall structure of a coherent orbital stream. Therefore, we conclude that while it is possible that either the Arches or Quintuplet could have formed on the open stream proposed by KDL15, it is unlikely that both clusters could have formed this way due to the difference in their orbits.

7.2.3. Star Formation along the Dust Lanes

Sormani et al. (2020b) find that star formation can also occur along the dust lanes before the x_1 – x_2 collisions take place. This has been invoked to explain the formation of the Sgr E complex, which comprises H II regions located at projected distances of \sim 170 pc from the GC that exhibit $-220 \, \mathrm{km \, s^{-1}} \lesssim v_{\mathrm{los}} \lesssim -190 \, \mathrm{km \, s^{-1}}$ (Anderson et al. 2020). We do not find evidence that this formation mechanism could produce either the Arches or Quintuplet cluster, as it would require highly eccentric prograde orbits with larger values of v_{los} at their current location than is observed ($|v_{\mathrm{los}}| \gtrsim 150 \, \mathrm{km \, s^{-1}}$, based on Figure 13 of Anderson et al. 2020). While highly eccentric orbits are possible for a small fraction of retrograde orbits (see

Figures 7 and 8), it is unclear how a retrograde orbit could be produced by this mechanism.

7.3. The Clusters are Unlikely to Merge with the NSC or YNC

Given the strong tidal field at the GC, the Arches and Quintuplet clusters are not expected to have long lifetimes before being tidally disrupted. N-body simulations predict that massive clusters with Galactocentric radii between 30–150 pc should tidally disrupt within ~ 20 Myr (Kim et al. 1999, 2000; Portegies Zwart et al. 2002). However, dynamical friction can cause clusters to inspiral closer to Sgr A*, potentially driving mergers with the NSC (half-light radius \sim 4.2 pc; Schödel et al. 2014) or even the YNC ($r \lesssim 0.5$ pc; Støstad et al. 2015). Indeed, it has been proposed that the inward migration of massive clusters could contribute significant mass to the NSC (e.g., Antonini et al. 2012; Arca Sedda et al. 2020) or be the source of the young stars found in the YNC (e.g., Gerhard 2001). Here we examine whether the Arches or Quintuplet clusters could undergo such mergers within their lifetimes.

Our results (which ignore dynamical friction and tidal disruption) show that the Arches and Quintuplet are allowed to be on orbits that bring them as close as ~25–30 pc from Sgr A* (Figure 9). Kim & Morris (2003) simulate massive clusters at similar radii and evaluate how close they migrate toward Sgr A* before disrupting. They find that only $10^6~M_{\odot}$ clusters with central densities of $\rho_c \gtrsim 10^6~M_{\odot}~\rm pc^{-3}$, or $10^5~M_{\odot}$ clusters with initial radii of 10 pc and similar or higher central densities, can bring significant numbers of stars into the YNC or NSC before dissolving. At $\sim 10^4~M_{\odot}$, the Arches and Quintuplet are one to two orders of magnitude less massive than these models and have central densities at least an order of magnitude lower as well (Arches $\rho_c = 2.0 \pm 0.4 \times 10^5~M_{\odot}~\rm pc^{-3}$; Espinoza et al. 2009). Therefore, it appears unlikely that either the Arches or Quintuplet will merge with either the NSC or YNC before being tidally disrupted, even if they are at the innermost orbits allowed by our analysis.

7.4. Orbit Analysis Using Different Gravitational Potentials

A significant assumption in our analysis of the cluster orbits is the gravitational potential of the GC. As discussed in Section 5.4, we adopt the potential from Kruijssen et al. (2015): An axisymmetric potential with the enclosed mass distribution from Launhardt et al. (2002) that is flattened in the z direction. We refer to this as the L02_flat potential. However, Sormani et al. (2020a, hereafter S20) present three alternative potentials for the inner \sim 300 pc of the galaxy based on axisymmetric Jeans modeling of the NSD. To examine the sensitivity of our results to the gravitational potential, we repeat our analysis with these alternative potentials in Appendix E and summarize the results here.

While the choice of gravitational potential does impact the orbital properties of the clusters, the effect is relatively small. For the Arches cluster, the S20 potentials produce orbits that do not extend as close to Sgr A* and are slightly more eccentric. The 3σ lower limits on the closest approach distance to Sgr A* are between $\sim\!25\text{--}50\,\mathrm{pc}$, compared to 24.7 pc for the L02_flat potential. The ratio $r_{\mathrm{apo}}/r_{\mathrm{peri}}$ has average (50th percentile) values between $\sim\!2.0\text{--}2.5$, compared to 1.9 for the L02_flat potential. For the Quintuplet cluster, the effect of the S20 potentials on the closest approach to Sgr A* is opposite

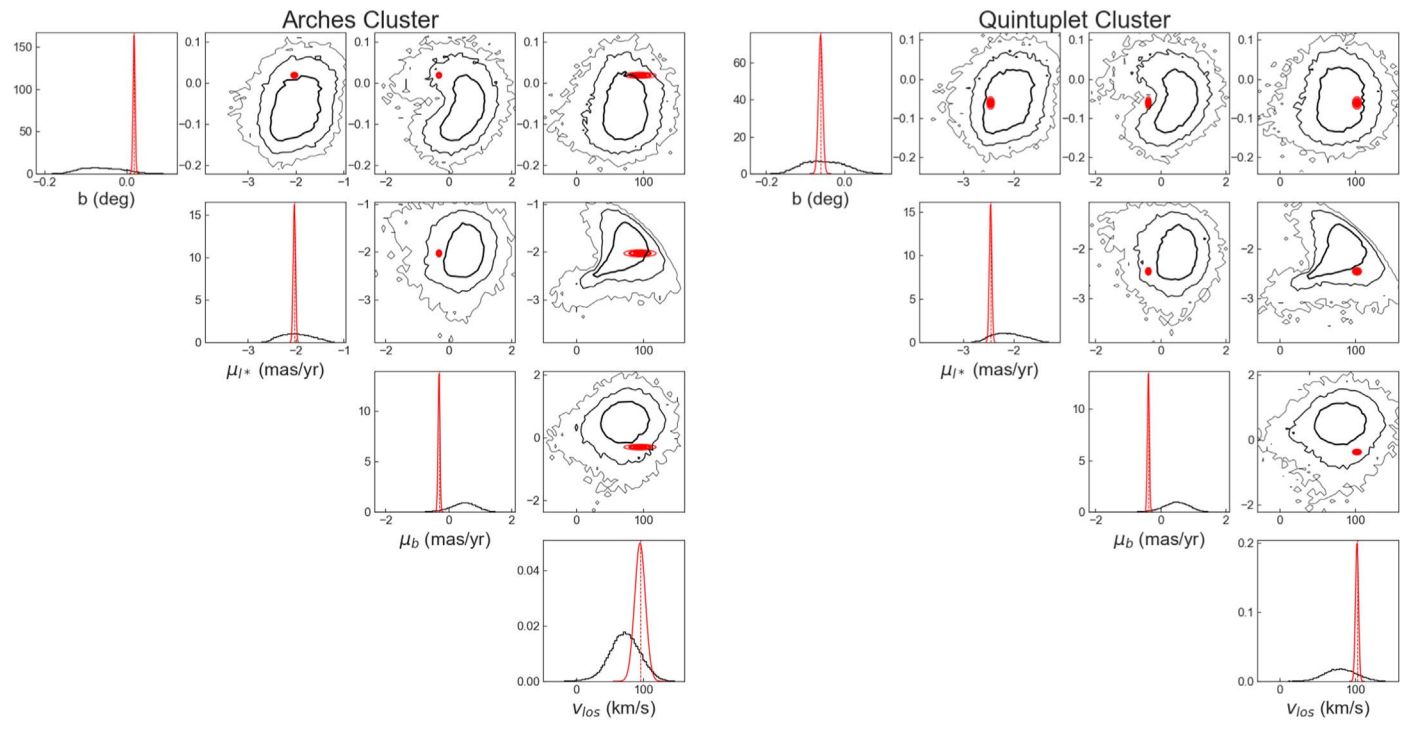


Figure 15. Comparison between the observed values of x_{int} for the Arches (left) and Quintuplet (right) clusters and their predicted values at the stream 1 intersection points on the KDL15 orbit. In all plots, the cluster measurements are in red and the predicted orbit values are in black. In the 2D contour plots, the thick, moderate, and thin lines correspond to the 1σ , 2σ , and 3σ probability contours, respectively. We find the clusters to be marginally consistent with stream 1, with the observations matching the orbit predictions within 2.71σ and 2.57σ for the Arches and Quintuplet, respectively.

compared to the Arches; the 3σ lower limits are closer (\sim 13–25 pc) than for the L02_flat potential (29.8 pc). However, the effect on $r_{\rm apo}/r_{\rm peri}$ is similar, with the Quintuplet orbits also having average values between \sim 2.0–2.5. Overall, we find that the choice of gravitational potential does not alter our results that neither cluster will pass close enough to Sgr A* to merge into the NSC within their lifetimes and that the clusters are inconsistent with a circular orbit.

To determine the robustness of the result that the clusters do not share a common orbit, we repeat the calculation in Equation (9) for the different gravitational potentials. The Arches always exhibits larger vertical oscillations in the Galactic Plane, and $P(b_{\max, \operatorname{arch} = \operatorname{quint}}) \leqslant 0.2\%$ for all potentials. Thus, the clusters do not share a common orbit for all choices of gravitational potentials examined here.

In addition, the choice of potential does not impact our conclusions regarding the viability of the cluster formation scenarios discussed in Section 7.2. The constraints on the cluster birth locations do not significantly change across the different potentials, and so there is a significant probability that the clusters formed in the regions of enhanced star formation predicted by the x_1 – x_2 gas collision scenario in all cases. ¹⁷ The choice of potential has a larger influence on the birth v_{los} of the clusters, especially at negative galactic longitudes. However, there is little evidence that the clusters exhibit an enhanced birth v_{los} compared to the x_2 gas orbits, with the possible exception of the Quintuplet cluster in the S20_2 potential, which may show a possible enhancement near $-200 \, \text{pc} <$

l < -150 pc. Thus, our conclusion that our results provide mild support for the x_1 – x_2 formation scenario remains unchanged.

For the open stream formation scenario, we note that the KDL15 orbit was derived assuming the Kruijssen et al. (2015) potential. Thus, changing the potential would naturally change the orbit model. However, recalculating the KDL15 orbit for different potentials is beyond the scope of this paper. That said, the Arches and Quintuplet clusters do not share a common orbit regardless of the potential used, and so this remains as a challenge for the open stream formation scenario.

8. Conclusions

We use multiepoch HST WFC3-IR observations and the Gaia EDR3 catalog to measure the absolute proper motion of the Arches and Quintuplet clusters and constrain their orbital properties. Using 26–28 Gaia stars in each field, we transform the HST astrometry into the Gaia reference frame (which is tied to the ICRF) and calculate absolute proper motions for $\sim\!35,000$ stars in the Arches field and $\sim\!40,000$ stars in the Quintuplet field, achieving a depth of F153M $\sim\!23$ mag in both. Using these catalogs, we measure bulk proper motions of $(\mu_{\alpha*},\ \mu_{\delta})_{\rm ICRF} = (-0.80 \pm 0.032,\ -1.89 \pm 0.021)$ mas yr $^{-1}$ for the Arches cluster and $(\mu_{\alpha*},\ \mu_{\delta})_{\rm ICRF} = (-0.96 \pm 0.032,\ -2.29 \pm 0.023)$ mas yr $^{-1}$ for the Quintuplet cluster. The uncertainties on these measurements are $\gtrsim\!5x$ smaller than previous work and are dominated by the construction of the reference frame.

For each cluster, we forward-model the set of orbits within the CMZ that can replicate its observed position and motion while taking into account the uncertainties in the cluster's present-day line-of-sight distance (d_{los}), age, and observational measurements. The posterior probability distributions for the birth positions and birth velocities of the clusters are highly

 $[\]overline{17}$ This statement assumes that the locations of x_1 – x_2 collision regions do not significantly change for the different potentials examined here, as well. Exploring the impact of the potential on the locations of x_1 – x_2 collision regions is beyond the scope of this paper.

degenerate, primarily due to the uncertainty in $d_{\rm los}$. Two solution modes are found for each cluster, one representing prograde orbits and the other representing retrograde orbits relative to the general gas flow in the CMZ. The retrograde orbits are deemed unlikely due to a lack of evidence (in either observations or simulations) for gas on retrograde orbits in the CMZ that might be capable of forming a cluster similar to the Arches or Quintuplet. Therefore, we restrict our analysis to the prograde solution mode only.

From the distribution of possible prograde orbits for the clusters, we find that:

- 1. The Arches and Quintuplet will not approach closer than 24.7 pc and 29.8 pc to Sgr A*, respectively. These values represent the 3σ lower limits on the distributions of closest approach distances. While this calculation ignores dynamical friction, previous simulations suggest that neither cluster will merge with the NSC or YNC before they are tidally disrupted (Kim & Morris 2003).
- 2. Both clusters are inconsistent with a circular orbit, with a 3σ lower limit on $r_{\rm apo}/r_{\rm peri}$ of ~ 1.4 . The orbits have a typical (i.e., 50th percentile) value of $r_{\rm apo}/r_{\rm peri} \sim 1.9$, which is equivalent to an orbital eccentricity of ~ 0.31 .
- 3. The clusters do not share a common orbit, as the Arches exhibits significantly larger vertical oscillations in the Galactic Plane than the Quintuplet.

These results are not significantly altered by the choice of gravitational potential.

The distribution of cluster orbits is examined in the context of two proposed formation scenarios for the clusters: the x_1 – x_2 collision scenario, in which the clusters formed when infalling gas from x_1 orbits collided with gas on x_2 orbits in the CMZ (e.g., Stolte et al. 2008, 2014), and the open stream scenario, where the clusters formed from the collapse of molecular clouds along the proposed KDL15 orbit (e.g., Kruijssen et al. 2015, 2019).

We conclude that our constraints on the birth position and location of the clusters are in mild agreement with the x_1 – x_2 scenario. The birth locations of the clusters are consistent with the expected region of enhanced star formation due to gas collisions, although the uncertainties are large. We do not find evidence that either cluster formed with an enhanced line-of-sight velocity (v_{los}) compared to typical x_2 gas orbits, as might occur due to momentum transfer from the higher-velocity x_1 cloud during a collision. However, this does not yet discount the x_1 – x_2 scenario, as the significance of this effect likely depends on several factors (e.g., the collision geometry and relative densities of the clouds). Thus, additional work is needed to determine if a v_{los} enhancement would be observable.

On the other hand, our results present a challenge for the open stream formation scenario. While the present-day positions and motions of the clusters are marginally consistent with their predicted values on "stream 1" of the KDL15 orbit individually, it is unclear how both clusters could have formed this way given the difference between their orbits. This would require the individual clouds on the KDL15 stream to span an intrinsic range of orbits that encompasses the difference in vertical oscillation between the clusters and yet still maintain the appearance of an orbital stream.

Future progress on constraining the formation mechanism(s) for the Arches and Quintuplet clusters can be made by reducing the uncertainties in several key areas. For the clusters

themselves, improved constraints on $d_{\rm los}$ would reduce the range of allowed orbits and thus provide more stringent constraints on their orbital properties, birth positions, and birth velocities. Further, the evaluation of whether the present-day position and motion of the clusters are consistent with the KDL15 orbit is dominated by the uncertainty KDL15 orbit itself. Reducing the uncertainty of the orbit model would provide a stronger test of whether the individual clusters are indeed consistent with forming via the open stream scenario. Finally, the GC gravitational potential itself remains a source of uncertainty, which impacts both the orbits of the clusters as well as the predictions of the different star formation scenarios.

The authors thank Jesus Salas, Mattia Sormani, and Perry Hatchfield for helpful discussions regarding the gravitational potential and possible star formation mechanisms at the Galactic center as well as the anonymous referee whose feedback improved this paper. M.W.H. is supported by the Brinson Prize Fellowship. This work was supported by HST AR-16121 and is based on observations made with the NASA/ ESA Hubble Space Telescope, obtained at the Space Telescope Science Institute, which is operated by the Association of Universities for Research in Astronomy, Inc., under NASA contract NAS 5-26555. The observations are associated with programs GO-11671, GO-12318, GO-12667, and GO-14613. This work used computational and storage services associated with the Hoffman2 Shared Cluster provided by UCLA Institute for Digital Research and Education's Research Technology Group and made extensive use of the NASA Astrophysical Data System.

Facilities: HST (WFC3-IR), Gaia.

Software: AstroPy (Astropy Collaboration et al. 2013, 2018), numPy (Oliphant 2006), Matplotlib (Hunter 2007), SciPy (Virtanen et al. 2020), KS2 (Anderson et al. 2008), galpy (Bovy 2015), Multinest (Feroz & Hobson 2008; Feroz et al. 2009), PyMultinest (Buchner et al. 2014).

Appendix A Testing the Proper-motion Catalogs

To check the proper motions in the Arches and Quintuplet field catalogs, we examine the distribution of the χ^2 values and astrometric residuals for the proper-motion fits. The χ^2 statistic is a measure of how large the proper-motion fit residuals are relative to the astrometric errors. For each star, the χ^2 statistic is calculated as

$$\chi^2 = \sum_{i=0}^{i=N} \frac{(x_{\text{obs}_i} - x_{\text{pred}_i})^2}{\sigma_{ast_{x_i}}^2},$$
 (A1)

where x_{obs_i} and x_{pred_i} are the observed and predicted position of the star in the *i*th epoch, $\sigma_{\text{ast}_{x_i}}$ is the astrometric error in the *i*th epoch, and N is the total number of epochs.

The distribution of χ^2 values for both cluster fields is shown in Figure 16. The distributions are found to be similar to the expected distribution in both the α^* and δ directions, indicating that the astrometric errors are a good representation of the fit residuals. There is a slight overabundance of stars with high χ^2 values for both clusters, which are dominated by fainter sources. This is likely due to systematic errors in the astrometry caused by stellar crowding, which impacts fainter sources more strongly than brighter sources.

Within a given epoch, the distribution of proper-motion fit residuals reveals whether there are systematic offsets in the astrometry that are not captured by the transformations. If significant, these offsets, which we refer to as residual distortion, could indicate that more complex transformations are required to correct the distortions in the field. Figure 17 shows the average ratio of proper-motion fit residuals to the astrometric error for

bright stars (F153M < 17.5 mag) in the Arches and Quintuplet fields for each epoch. Bright stars are used for this analysis because their astrometric errors are the smallest, thus making them the most sensitive to residual distortion. We find that the average residual distortion is less than half of the bright-star astrometric errors in all epochs and conclude that residual distortion does not significantly impact our measurements.

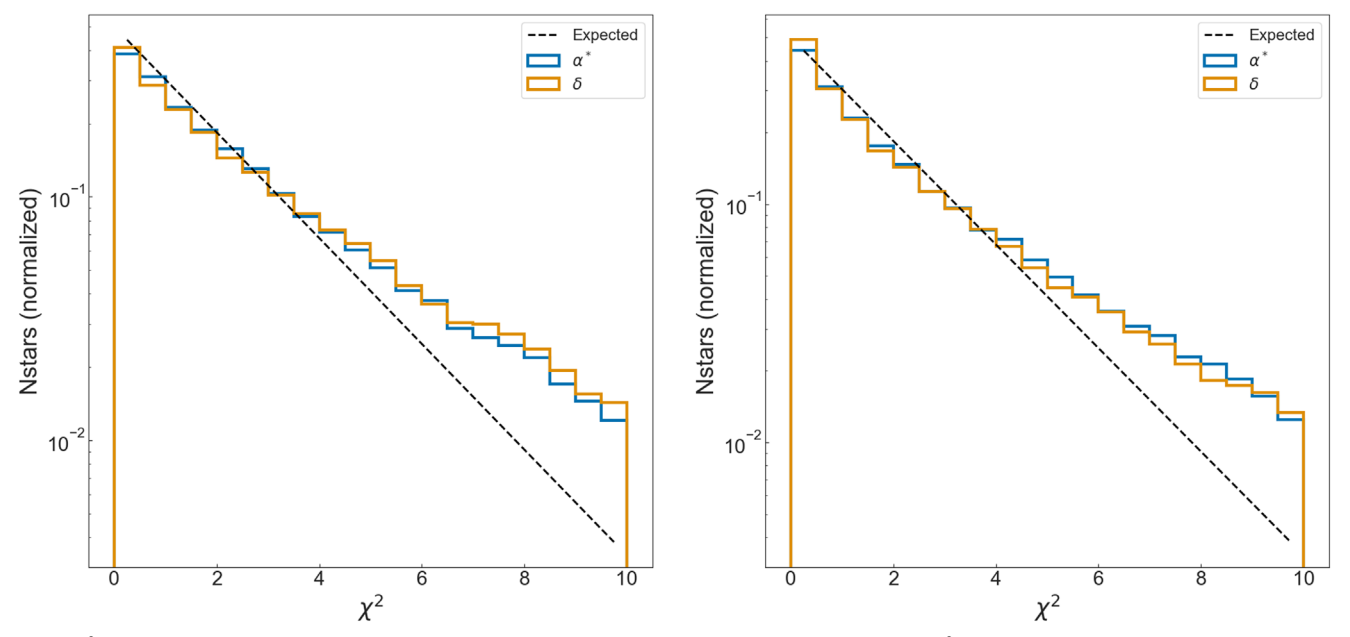


Figure 16. χ^2 distributions for the proper-motion fits in the Arches (left) and Quintuplet (right) catalogs. The χ^2 distribution in the α^* and δ directions (blue and orange lines, respectively) are similar to the expected χ^2 distribution with two degrees of freedom (black dotted line).

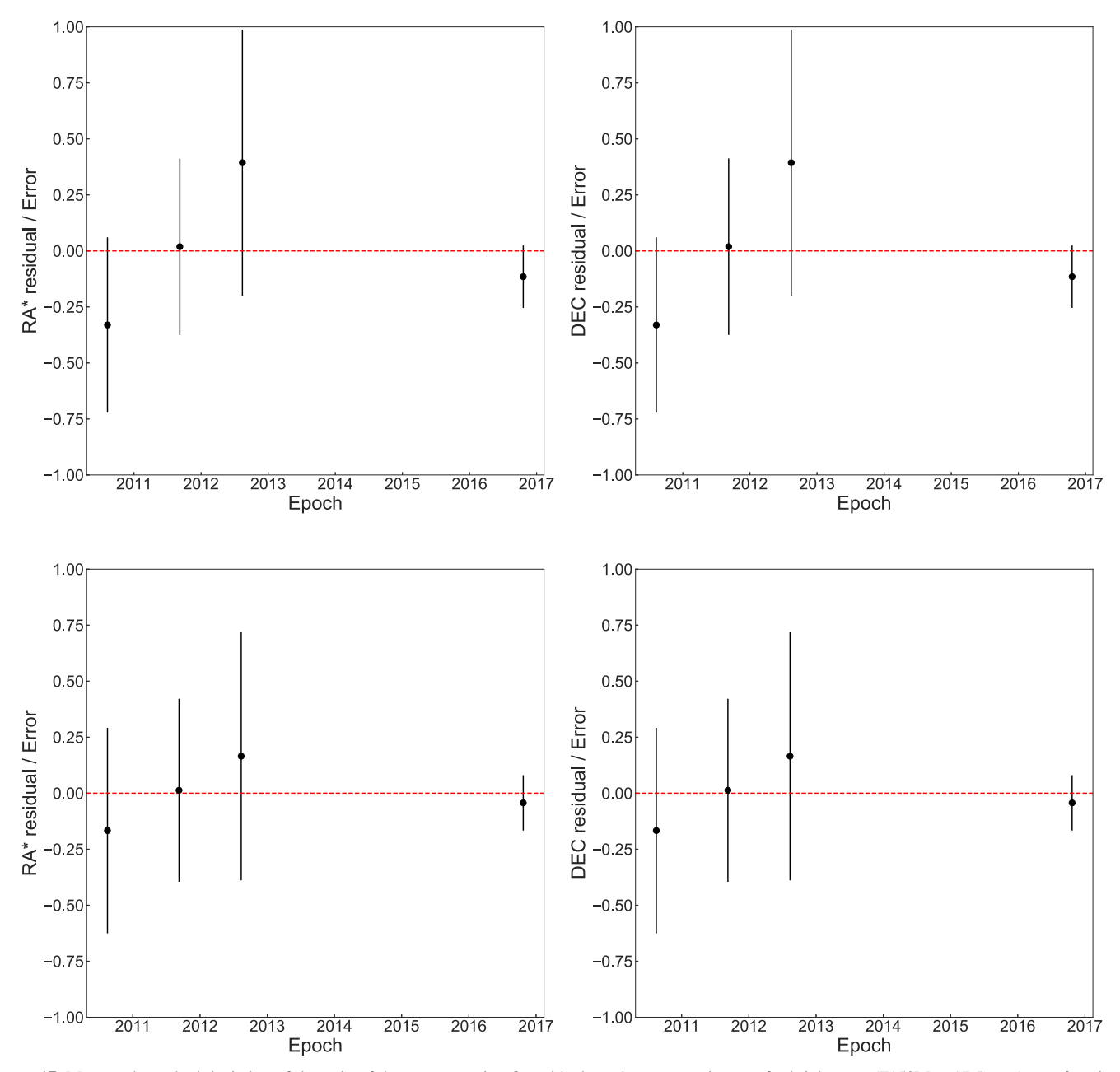


Figure 17. Mean and standard deviation of the ratio of the proper-motion fit residuals to the astrometric error for bright stars (F153M < 17.5 mag) as a function of epoch for the Arches (upper panels) and Quintuplet (lower panels) catalogs. The average residual is less than half of the astrometric error for all epochs and so we conclude that residual distortion does not significantly impact our measurements.

Appendix B Modeling Cluster and Field Star Proper Motions with Gaussian Mixture Models

Here we describe the methodology for modeling the cluster and field star proper motions using GMMs, report the parameters of the best-fit models for the Arches and Quintuplet clusters, and discuss how cluster membership probabilities are calculated for individual stars.

B.1. Gaussian Mixture Models: Methodology

We follow the methodology of R19 to find the GMM that best matches the data. Briefly, we use multiple Gaussians to describe the field star populations and a single Gaussian to

describe the cluster members. Each Gaussian used to describe the field population has six free parameters: the fraction of the total sample described by that Gaussian (π), the proper-motion centroid of the Gaussian (μ_{α^*} , μ_{δ} for the α^* and δ directions, respectively), the standard deviation along the semimajor axis (σ_a), the ratio between the semiminor and semimajor axis (f), and the angle between the semimajor axis and the α^* axis (θ). In contrast, the Gaussian used to describe the star cluster has only four free parameters (π , μ_{α^*} , μ_{δ} , σ_a), as we require it to be circular (e.g., f=1 and $\theta=0^\circ$). We adopt the same likelihood equation as R19 and use Multinest/PyMultinest to search the parameter space and calculate posterior probability distributions for the free parameters in the GMM.

Table 10
Arches Gaussian Mixture Model: Free Parameters, Priors, and Results

	Cluster	Gaussian	Field	Gaussian 1	Field	Gaussian 2	Field	Gaussian 3
Parameter	Prior	Result	Prior	Result	Prior	Result	Prior	Result
π_k	U(0, 1)	0.039 ± 0.003	U(0, 1)	0.46 ± 0.02	U(0, 1)	0.34 ± 0.02	U(0, 1)	0.16 ± 0.01
$\mu_{\alpha^*,k}$ (mas yr ⁻¹)	G(-0.8, 2)	-0.80 ± 0.01	U(-6, 6)	-2.43 ± 0.05	U(-6, 6)	-2.62 ± 0.06	U(-6, 6)	-1.41 ± 0.05
$\mu_{\delta,k}$ (mas yr ⁻¹)	G(-1.88, 2)	-1.89 ± 0.01	U(-6, 6)	-4.49 ± 0.08	U(-6, 6)	-4.84 ± 0.07	U(-6, 6)	-2.83 ± 0.05
$\sigma_{a,k}$ (mas yr ⁻¹)	U(0, 3)	0.08 ± 0.02	U(0, 8)	2.71 ± 0.05	U(0, 8)	3.26 ± 0.05	U(0, 8)	1.16 ± 0.06
f	•••	1.0	U(0, 1)	0.48 ± 0.02	U(0, 1)	0.93 ± 0.02	U(0, 1)	0.50 ± 0.04
θ_k (rad)	•••	0	$U(0, \pi)$	0.98 ± 0.02	$U(0, \pi)$	1.06 ± 0.13	$U(0, \pi)$	0.92 ± 0.04

Note. Description of parameters. π_k = fraction of stars in the Gaussian. $\mu_{\alpha^*,k} = \alpha^*$ velocity centroid of Gaussian. $\mu_{\delta,k} = \delta$ velocity centroid of the Gaussian. $\sigma_{a,k} = 0$ semimajor axis of the Gaussian. $\sigma_{a,k} = 0$ semimajor axis. $\sigma_{a,k} = 0$ semimajor axis. $\sigma_{a,k} = 0$ semimajor axis.

Description of priors: Uniform distributions: U(min, max), where min and max are bounds of the distribution; Gaussian distributions: $G(\mu, \sigma)$, where μ is the mean and σ is the standard deviation.

Table 11
Quintuplet Gaussian Mixture Model: Free Parameters, Priors, and Results

	Cluster	Gaussian	Field	Gaussian 1	Field	Gaussian 2	Field Gaussian 3		
Parameter	Prior	Result	Prior	Result	Prior	Result	Prior	Result	
π_k	U(0, 1)	0.047 ± 0.003	U(0, 1)	0.53 ± 0.02	U(0, 1)	0.29 ± 0.02	U(0, 1)	0.13 ± 0.01	
$\mu_{\alpha^*,k}$ (mas yr ⁻¹)	G(-0.96, 2)	-0.96 ± 0.01	U(-6, 6)	-2.58 ± 0.04	U(-6, 6)	-2.70 ± 0.06	U(-6, 6)	-1.61 ± 0.06	
$\mu_{\delta,k}$ (mas yr ⁻¹)	G(-2.26, 2)	-2.29 ± 0.01	U(-6, 6)	-4.79 ± 0.06	U(-6, 6)	-4.97 ± 0.07	U(-6, 6)	-3.12 ± 0.07	
$\sigma_{a,k}$ (mas yr ⁻¹)	U(0, 3)	0.11 ± 0.012	U(0, 8)	2.44 ± 0.04	U(0, 8)	3.42 ± 0.06	U(0, 8)	1.20 ± 0.08	
f		1.0	U(0, 1)	0.49 ± 0.02	U(0, 1)	0.89 ± 0.02	U(0, 1)	0.42 ± 0.04	
θ_k (rad)	•••	0	$U(0, \pi)$	0.99 ± 0.01	$U(0, \pi)$	0.95 ± 0.07	$U(0, \pi)$	0.92 ± 0.03	

Note. Description of parameters. π_k = fraction of stars in the Gaussian. $\mu_{\alpha^*,k} = \alpha^*$ velocity centroid of Gaussian. $\mu_{\delta,k} = \delta$ velocity centroid of the Gaussian. $\sigma_{a,k} = \infty$ semimajor axis of the Gaussian. $f = \infty$ ratio of semiminor to semimajor axis. $\theta_k = \infty$ angle between $\sigma_{a,k}$ and the α^* axis. Description of priors: Uniform distributions: U(min, max), where min and max are bounds of the distribution; Gaussian distributions: G(μ , σ), where μ is the mean and

The priors used for the GMM parameters are given in Tables 10 and 11. For most parameters, we adopt uniform priors with the same minimum and maximum ranges as R19. The exception to this is the proper-motion centroid of the cluster Gaussian, for which we adopt a Gaussian prior with a mean equal to the median HST-Gaia proper motion of high-probability cluster members established via previous analyses (e.g., stars previously identified as having $P_{\rm clust} > 0.7$ in H19 and R19). We adopt a conservative standard deviation of 2 mas for the Gaussian priors, over $10 \times$ larger than the actual standard deviation of the proper-motion values for these stars, in order to minimize the influence of this prior on the final result.

 σ is the standard deviation.

The final choice to be made is the number of Gaussian components to use in the GMM. To do this, we repeat the analysis using three, four, and five total Gaussians and then use the Bayesian Information Criterion (BIC; Schwarz 1978) to identify which model represents the best fit of the data. The BIC strongly prefers the GMM with four components for both clusters.

B.2. Best-fit GMM Model Parameters

The best-fit parameters for the four-component GMMs for the proper-motion distribution in the Arches and Quintuplet fields are given in Tables 10 and 11, respectively. Note that these GMMs are different from the ones presented in H19 and R19 because (1) the proper motions in this paper are in an absolute reference frame (ICRF) rather than a relative one, and (2) the proper-motion uncertainties are larger as discussed in Section 3.3. However, the cluster membership probabilities we calculate in Appendix B.3 are generally consistent with those in H19 and R19 within 0.05.

B.3. Stellar Cluster Membership Probabilities

For each star, a cluster membership probability $P_{\rm clust}$ is calculated based on the best-fit GMM in the same manner as H19 and R19:

$$P_{\text{clust}} = \frac{\pi_c P_c}{\pi_c P_c + \sum_k^K \pi_k P_k},\tag{B1}$$

where π_c and π_k are the fraction of total stars in the cluster and kth field Gaussian, respectively, and P_c and P_k are the probability of the given star being part of the cluster and kth field Gaussian, respectively, based on its observed proper motion. If we consider stars with $P_{\rm clust} \geqslant 0.7$ to be high-probability cluster members, then we find that our sample includes 577 high-probability members for the Arches cluster

and 977 high-probability members for the Quintuplet cluster. If we sum the cluster membership probabilities, we obtain $\Sigma P_{\rm clust} = 1503.9$ for the Arches sample and $\Sigma P_{\rm clust} = 2238.5$ for the Quintuplet sample. The cluster membership probabilities are included in the proper-motion catalogs (Tables 3 and 4).

Appendix C Full Posteriors for Cluster Orbit Models

The posterior probability distributions for the free parameters in the Arches and Quintuplet orbit models are shown in Figures 18 and 19, respectively.

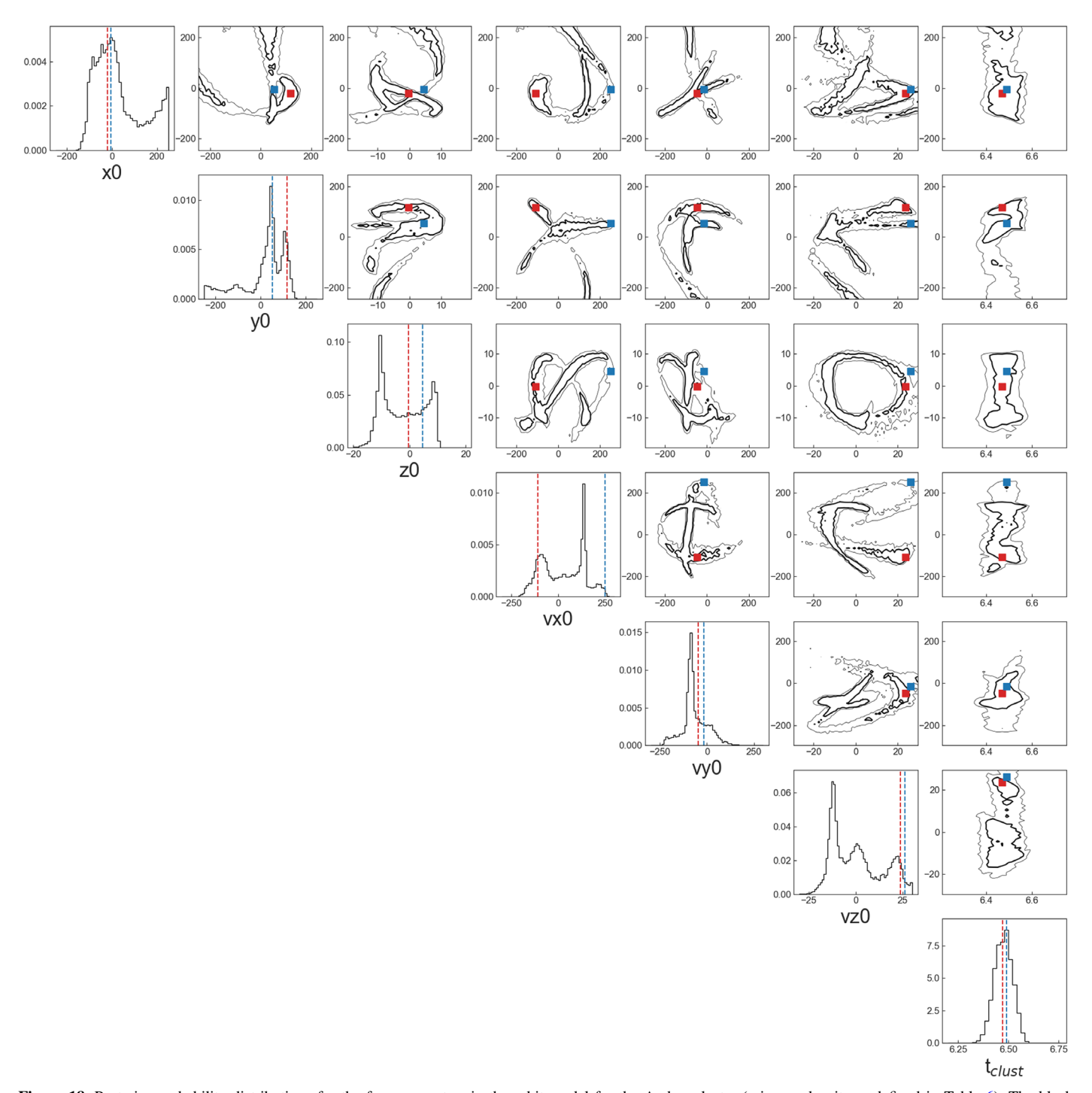


Figure 18. Posterior probability distributions for the free parameters in the orbit model for the Arches cluster (priors and units as defined in Table 6). The black histograms show the marginalized one-dimensional posterior for a given parameter, while the black contours show the 1σ (thick) and 2σ (thin) contours for the joint posteriors. The dotted lines and squares represent the values of the maximum likelihood orbit in each solution mode for the one-dimensional and joint posterior plots, respectively, with the red color corresponding to mode 1 and the blue color corresponding to mode 2.

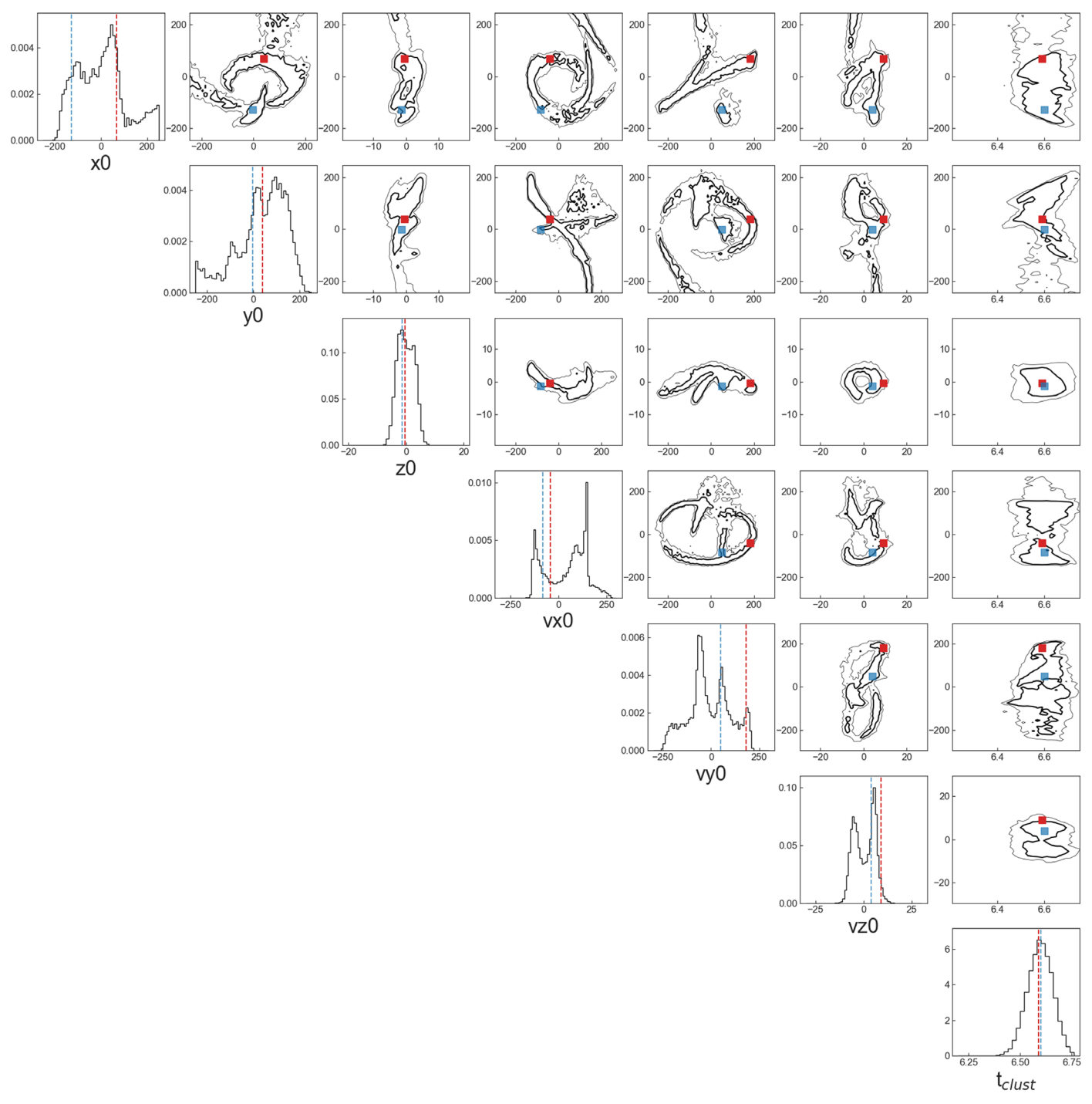


Figure 19. Posterior probability distributions for the free parameters in the orbit model for the Quintuplet cluster, constructed in the same manner as Figure 18.

Appendix D KDL15 Analysis

D.1. Calculating the Uncertainty in the KDL15 Orbit Model

Because of the uncertainty in $d_{\rm los}$, there are three possible locations of the Arches and Quintuplet clusters on the KDL15 orbit based on their galactic longitudes (Figure 14). In Section 7.2.2, we calculate the probability that the clusters are at these locations by comparing the present-day cluster galactic latitude and motion $(b, \mu_{l*}, \mu_b, \text{ and } v_{los})$ to their

predicted values on the KDL15 orbit. We use orbit simulations to determine the uncertainty in the KDL15 orbit model, which is a key component of this analysis.

First, we construct the same gravitational potential for the GC that is used by KDL15. This potential is based on the enclosed mass distribution for the inner 300 pc of the Milky Way from Launhardt et al. (2002), but is flattened in the vertical direction by a factor q_{ϕ} :

$$\Phi(x, y, z) = \Phi_S(r(q_\phi)), \tag{D1}$$

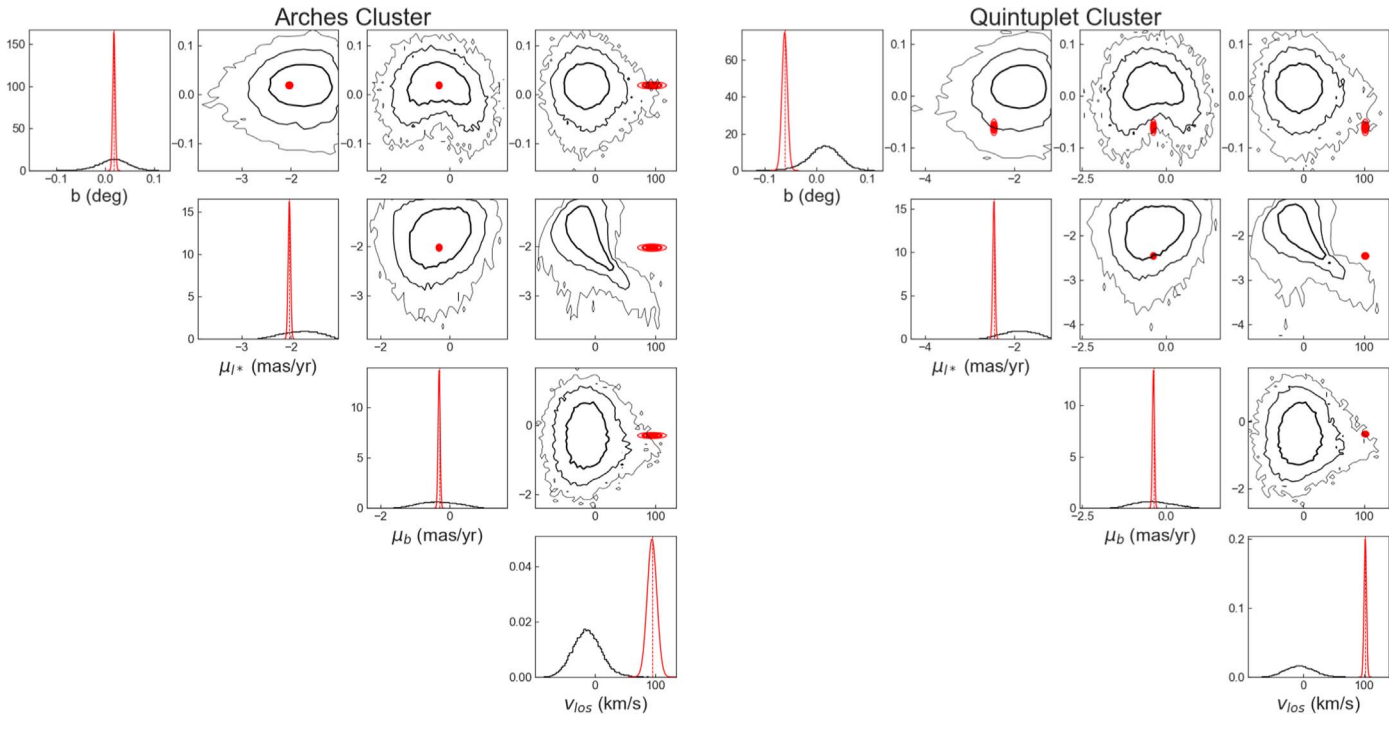


Figure 20. The comparison between the observed values of x_{int} for the Arches (left) and Quintuplet (right) clusters compared to the predicted values for stream 2 of the KDL15 orbit. The plots are constructed in the same manner as in Figure 15. The Arches and Quintuplet are discrepant with stream 2 by 4.25σ and 4.94σ , respectively.

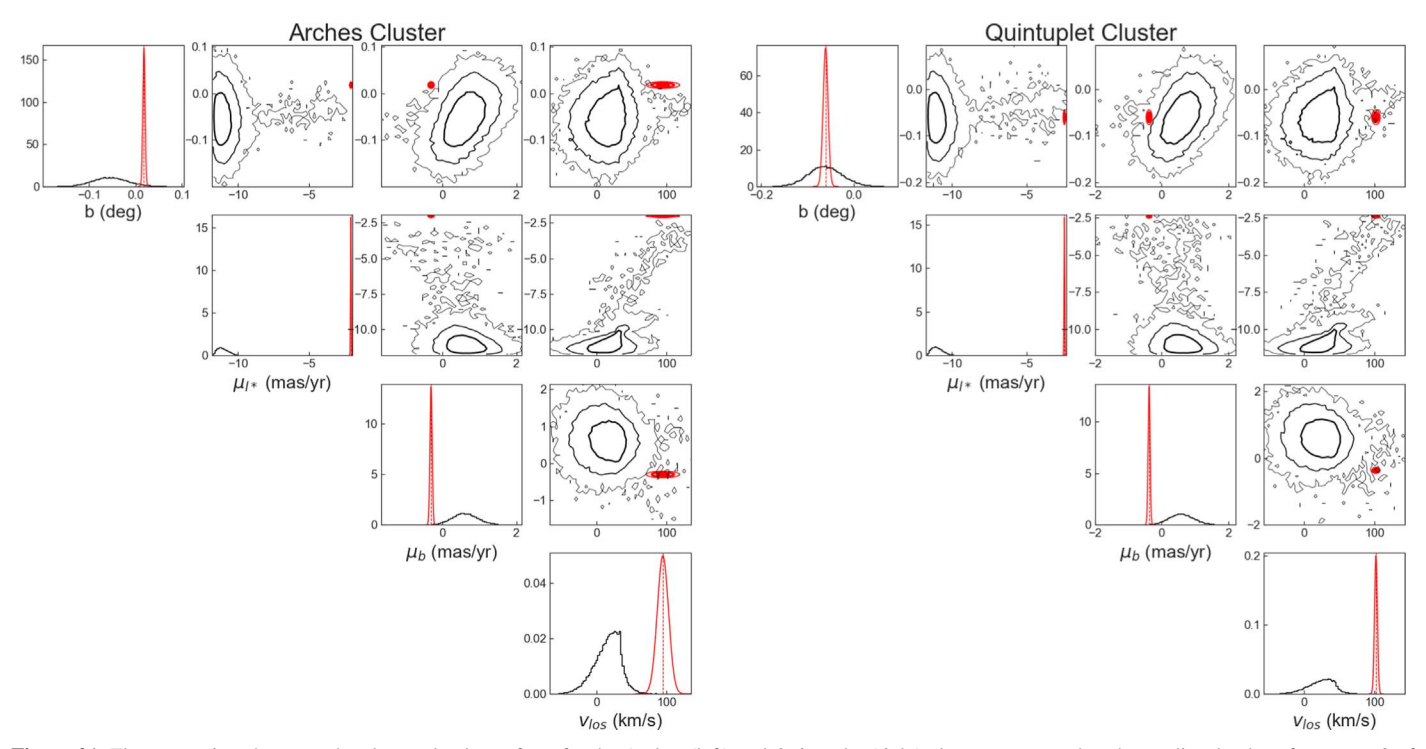


Figure 21. The comparison between the observed values of x_{int} for the Arches (left) and Quintuplet (right) clusters compared to the predicted values for stream 3 of the KDL15 orbit. The plots are constructed in the same manner as in Figure 15. The Arches and Quintuplet are discrepant with stream 3 by $>10\sigma$.

where $\Phi_S(r(q_\phi))$ is a spherical potential calculated at the modified radius:

$$r(q_{\phi})^2 = x^2 + y^2 + \frac{z^2}{q_{\phi}^2}.$$
 (D2)

KDL15 require a flattened potential in order to produce the vertical oscillations in their orbit model. They fit q_{ϕ} as a free parameter in their analysis, obtaining $q_{\phi}=0.63^{+0.07}_{-0.06}$. While q_{ϕ} is not well constrained by direct measurements, models of the structure of the Galactic bulge are significantly flattened in the z direction (e.g., Rodriguez-Fernandez & Combes 2008; Wegg & Gerhard 2013), suggesting that a flattened potential is not an unreasonable assumption.

The KDL15 orbit is parameterized by six parameters: the apoapse and periapse (R_a and R_p), the height above the galactic plane (z_p) , the velocity angle at pericenter (θ_{kdl}) , the projection angle between the origin-observer and origin-pericenter vectors (ϕ) , and the ratio of the vertical-to-planar axes of the gravitational potential (q_{ϕ}) . We draw 50,000 sets of these parameters from Gaussian distributions, each with a mean and standard deviation equal to the corresponding best-fit values and uncertainties reported in Table 1 of KDL15.18 From these parameters we calculate the three-dimensional position and velocity of a particle at periapse for each of the orbits. We then integrate the orbits for ± 2.5 Myr from periapse (the same time range as KDL15) with a time step of 0.025 Myr using galpy, each with a gravitational potential flattened by a value for q_{ϕ} that is also drawn from a Gaussian distribution with a mean and standard deviation corresponding to the constrain reported in KDL15.

We use this set of orbits to calculate the uncertainty in the predicted position and motion of the KDL15 orbit at each of the intersection points in Figure 14. First, we convert the orbit positions and velocities at each time step from galpy Galactocentric coordinates into observed quantities (l_{kdl} , b_{kdl} , $\mu_{l*,kdl}$, $\mu_{b,kdl}$, $\nu_{los,kdl}$) using the distance, location, proper motion, and radial velocity of Sgr A* as described in Section 5. Next, we linearly interpolate b_{kdl} , $\mu_{l*,kdl}$, $\mu_{b,kdl}$, and $\nu_{los,kdl}$ as a function of l_{kdl} in order to get their values at each intersection point. The mean and standard deviation of a given quantity across all 50,000 orbits thus represent its predicted value and uncertainty in the KDL15 orbit model.

D.2. Cluster Comparison to KDL15 Streams 2 and 3

Figures 20 and 21 show a comparison between the observed values of $x_{\rm int}$ for the clusters and their corresponding predicted values at the Stream 2 and 3 intersection points, respectively. The KDL15 orbit predictions for both streams are significantly different from the observations: Stream 2 is discrepant by 4.35σ and 5.03σ for the Arches and Quintuplet, respectively, and stream 3 is discrepant by $>10\sigma$ for both clusters. For Stream 2, the largest discrepancy is found in the $v_{\rm los}$ dimension; the observed values for the clusters are significantly higher than what the KDL15 orbit calls for. For Stream 3, the observed values for μ_{l*} are in the opposite direction to what is predicted by the KDL15 orbit.

Appendix E Orbit Constraints Using Different GC Gravitational Potentials

We repeat the orbit analysis described in Section 5 using the three alternative gravitational potentials for the GC proposed by Sormani et al. (2020a, hereafter \$20). These potentials have two components, one for the NSC and the other for the NSD. The NSC component is the same for each potential, generated from the axisymmetric cluster model of Chatzopoulos et al. (2015). Each NSD component has a different functional form for the mass distribution: the best-fit model from Launhardt et al. (2002) (Equation (24) from \$20), the best-fit model from Chatzopoulos et al. (2015) (Equations (25) and (26) from \$20), and a deprojection of the stellar density profile from Gallego-Cano et al. (2020) (Equation (27) from \$20). We refer to these potentials as S20_1, S20_2, and S20_3, respectively. S20 fit a scale factor to the NSD component of each potential based on Jeans modeling of the NSD. We refer to the potential used in the main body of the paper as L02 flat, as it is a flattened version of the potential from the Launhardt et al. (2002) mass distribution.

The distributions of the closest approach distances and $r_{\rm apo}/r_{\rm peri}$ ratios for the prograde cluster orbits using the different potentials are shown in Figures 22 and 23 for the Arches and Quintuplet clusters, respectively. A summary of the limits of these properties for the different potentials is provided in Table 12. For the Arches, the 3σ lower limits for both the closest approach distance and $r_{\rm apo}/r_{\rm peri}$ for the S20 potentials are similar to or larger than the limits for the L02_flat potential. For the Quintuplet, the 3σ limits on the closest approach distance for the S20 potentials are smaller than for the L02 flat potential, but the 3σ limits on $r_{\rm apo}/r_{\rm peri}$ are larger. In general, this indicates that the S20 potentials produce orbits with generally higher eccentricities than the L02_flat potential for both clusters. Our conclusions that the Arches and Quintuplet clusters are unlikely to inspiral into the NSC and that they cannot be on circular orbits do not change when these different potentials are used.

We repeat the calculation in Equation (9) for the Arches and Quintuplet orbits in these different potentials to assess if the clusters could share a common orbit. Similar to the L02_flat potential, the Arches always exhibits larger vertical oscillations in the Galactic Plane, with $P(b_{\text{max,arch}=\text{quint}}) = 0.1\%$, 0.2%, and 0.01% for the S20_1, S20_2, and S20_3 potentials, respectively.

Table 12
Orbit Properties with Different Potentials

Cluster	Potential ^a	Closest Approach	Min Ratio	Ave Ratio
Arches	L02_flat	24.7	1.4	1.9
Arches	S20_1	24.4	1.7	2.2
Arches	S20_2	34.2	1.6	2.1
Arches	S20_3	50.0	2.2	2.9
Quintuplet	L02_flat	29.8	1.4	1.9
Quintuplet	S20_1	13.2	1.7	2.1
Quintuplet	S20_2	24.7	1.8	2.0
Quintuplet	S20_3	19.6	1.9	2.5

Notes. Description of columns. Potential: potential used. Closest approach: 3σ lower limit on closest approach to Sgr A* in parsecs. Min Ratio: 3σ lower limit of $r_{\rm apo}/r_{\rm peri}$. Ave Ratio: 50th percentile of $r_{\rm apo}/r_{\rm peri}$.

¹⁸ Some of the reported parameters have mildly asymmetric error bars. For these, we adopt a symmetric uncertainty that is equal to the average of the positive and negative error values.

^a Note that the L02_flat potential is used in the main text of the paper.

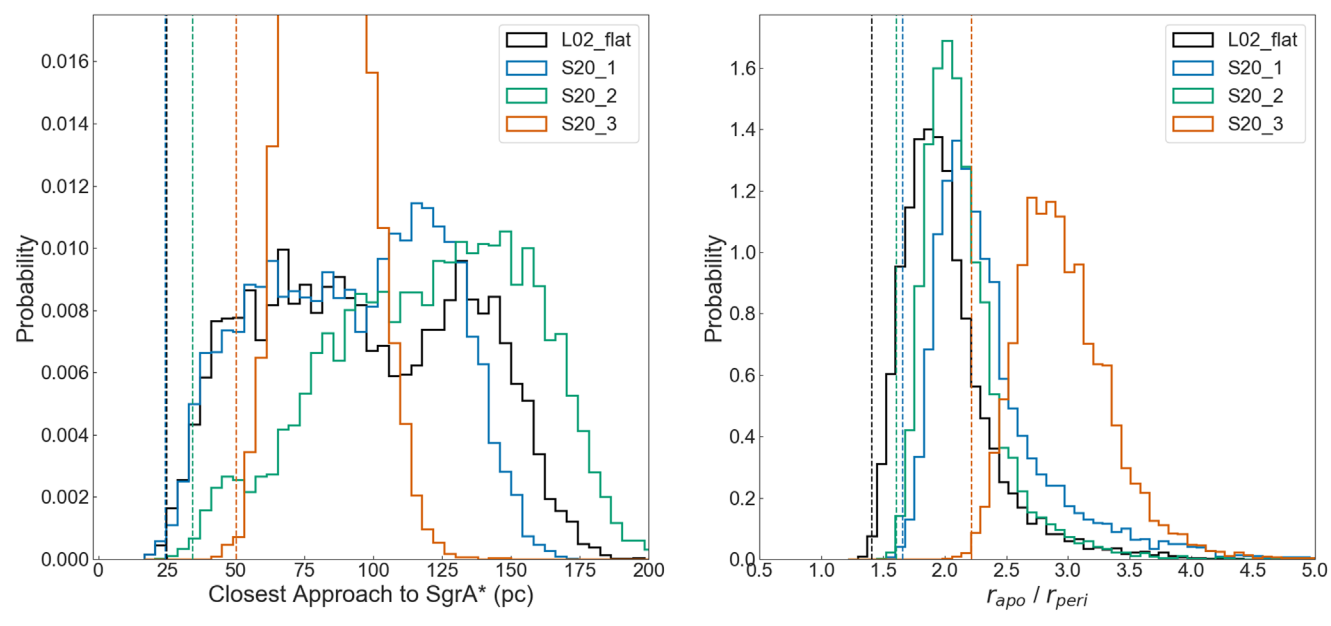


Figure 22. The probability distributions for the closest approach to Sgr A* (left) and $r_{\rm apo}/r_{\rm peri}$ (right) for prograde orbits of the Arches cluster using different gravitational potentials for the GC. The black histogram shows the results for the L02_flat potential that is adopted in the main text of the paper, while the different color histograms show the results for the S20_1, S20_2, and S20_3 potentials. The 3 σ lower limits of these properties for each potential are shown by the vertical dotted line with the same color as the corresponding histogram. The S20 potentials produce orbits that do not extend as close to Sgr A* and have larger $r_{\rm apo}/r_{\rm peri}$ ratios compared to the L02_flat potential. These differences do not change the conclusions drawn in this paper.

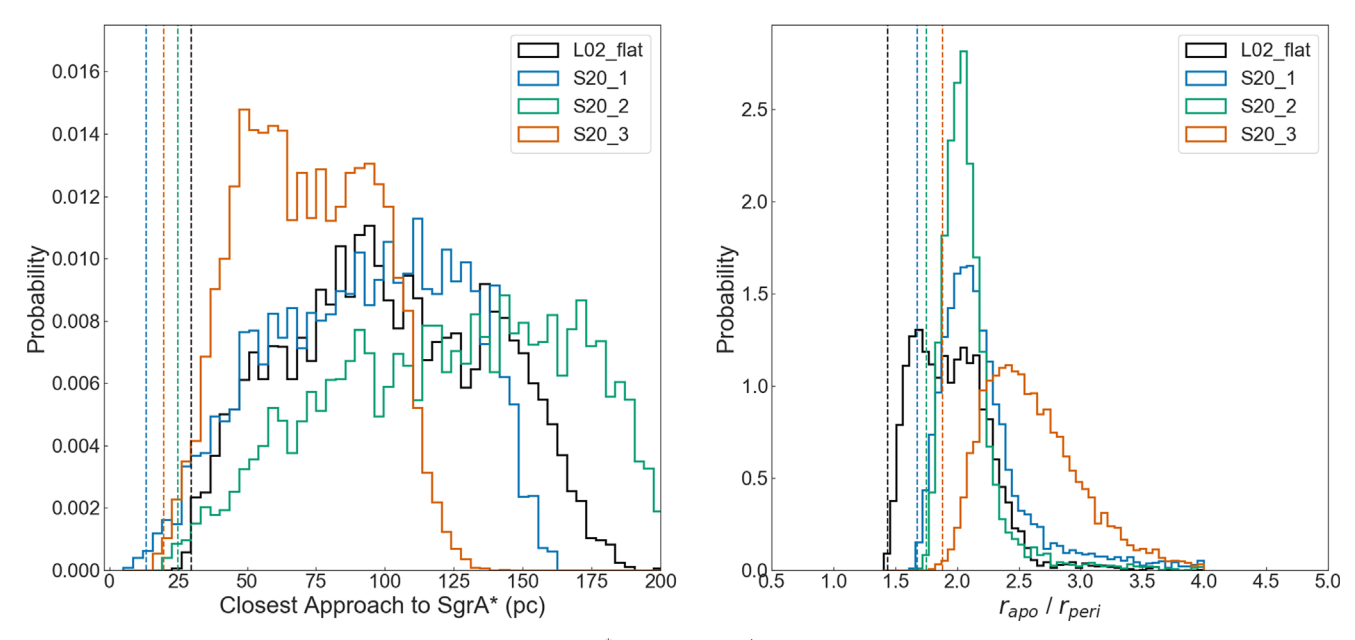


Figure 23. Probability distributions for the closest approach to Sgr A* (left) and $r_{\rm apo}/r_{\rm peri}$ (right) for prograde orbits of the Quintuplet cluster using different gravitational potentials for the GC, constructed in the same manner as Figure 22. The S20 potentials produce orbits that extend closer to Sgr A* and have higher eccentricities compared to the L02_flat potential. These differences do not change the conclusions drawn in this paper.

Thus, the choice of gravitational potential does not change our conclusion that the clusters do not share a common orbit.

We compare the constraints on the cluster birth locations and birth $v_{\rm los}$ for different potentials to the predictions of the x_1 – x_2 gas collision scenario in Figures 24 and 25. Changing the gravitational potential has a relatively minor effect on the cluster birth locations, as the uncertainty is primarily driven by the uncertainty in $d_{\rm los}$ rather than the potential itself. For all

potentials, both the Arches and Quintuplet have a significant probability of forming in the predicted regions of enhanced star formation in the x_1 – x_2 gas collision scenario. However, the gravitational potential appears to have a larger effect on the birth $v_{\rm los}$ of the clusters, especially at negative galactic longitudes. That said, we do not find evidence that either cluster formed with a higher $v_{\rm los}$ than typical x_2 gas velocities for most potentials. The exception is the $v_{\rm los}$ constraints for the

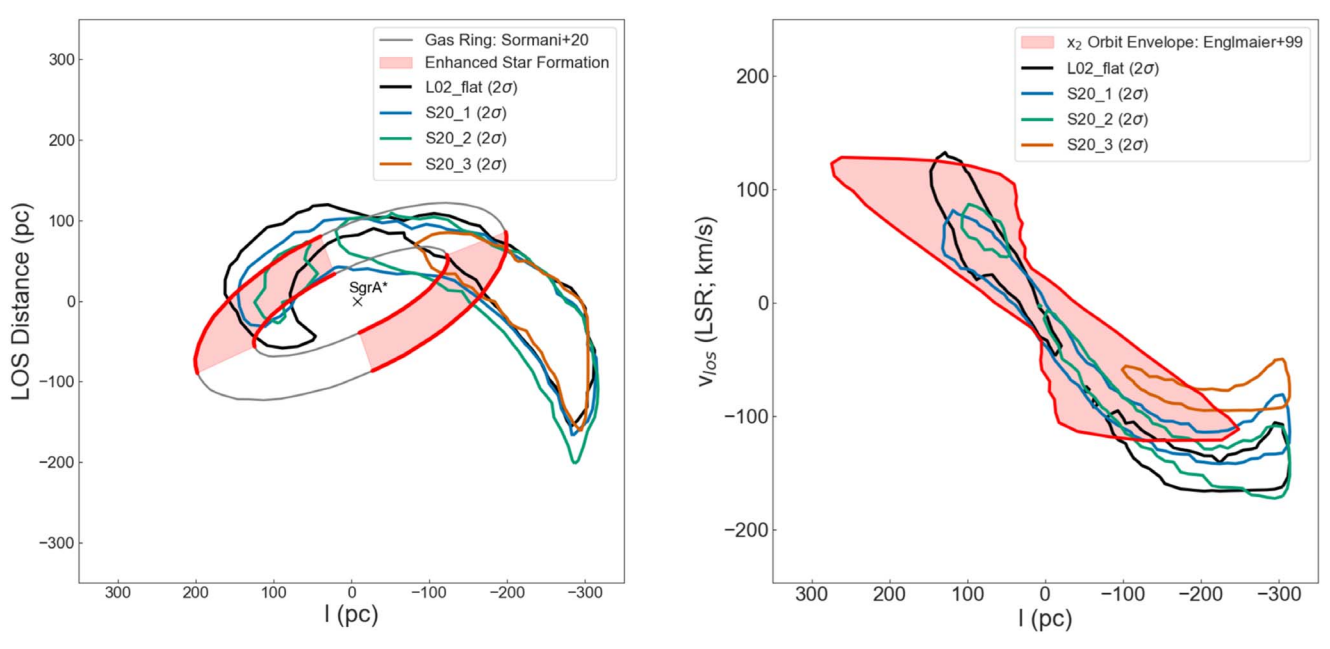


Figure 24. 2σ probability contours on the cluster birth location (left) and initial v_{los} (right) for the Arches cluster assuming different gravitational potentials, plotted similarly to Figures 12 and 13. In the left panel, we find that the Arches cluster has a significant probability of forming in the region of enhanced star formation predicted by the x_1 - x_2 collision scenario (red shaded region) regardless of the gravitational potential used. In the right panel, we find that there is no evidence that the cluster formed at a higher v_{los} than gas on x_2 orbits (red shaded region) for birth locations within the gas ring ($|l| \lesssim 200$ pc), regardless of the gravitational potential used. Our conclusion that these results are in mild support for the x_1 - x_2 collision scenario is not affected by the choice of gravitational potential.

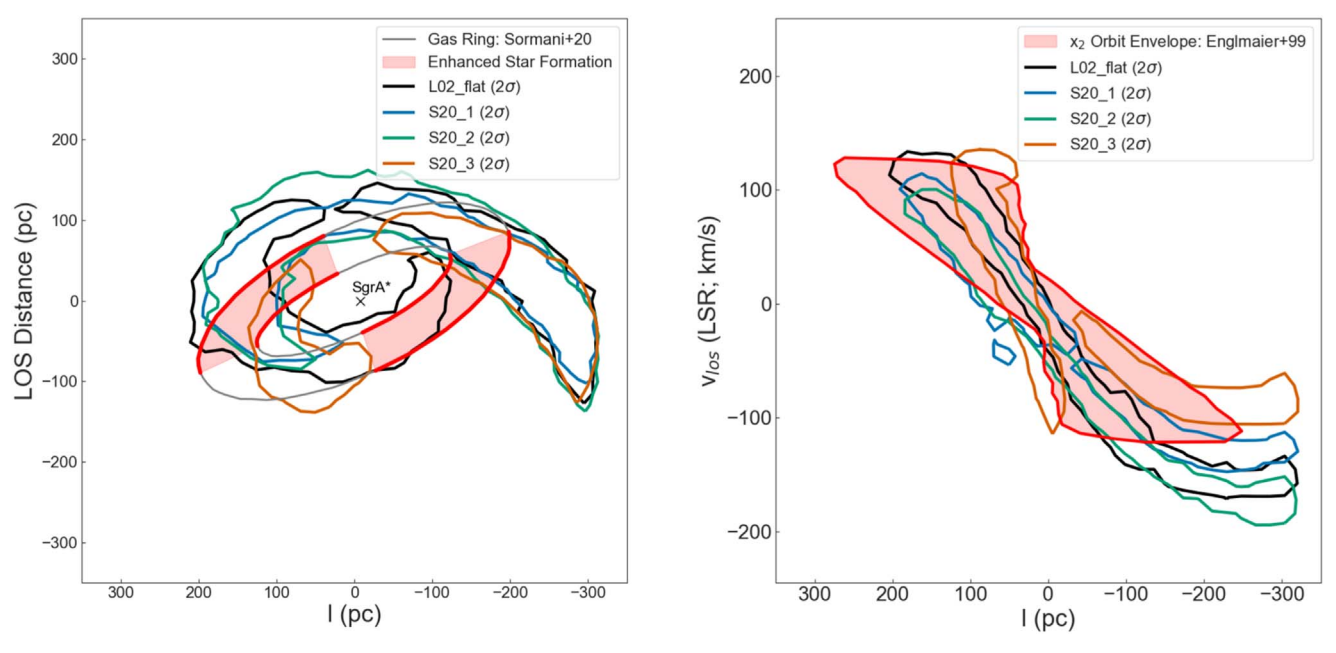


Figure 25. $.2\sigma$ probability contours on the cluster birth location (left) and initial v_{los} (right) for the Quintuplet cluster assuming different gravitational potentials, plotted similarly to Figure 24. The cluster birth location remains consistent with the x_1 - x_2 formation scenario for all potentials, and there is some evidence for an enhancement in the birth v_{los} relative to the x_2 orbits if the S20_2 potential is used. Our conclusion that these results are in mild support for the x_1 - x_2 collision scenario is not affected by the choice of gravitational potential and is perhaps strengthened if the S20_2 potential is used.

Quintuplet cluster using the S20_2 potential, which produces values that appear slightly enhanced compared to the x_2 gas orbits between $-200\,\mathrm{pc} \lesssim l \lesssim -150\,\mathrm{pc}$. Overall, our conclusion that the clusters are mildly consistent with the x_1 - x_2 formation scenario is not affected by the choice of gravitational potential and is perhaps strengthened for the Quintuplet cluster if the S20_2 potential is used given the potential v_{los} enhancement.

ORCID iDs

Matthew W. Hosek, Jr. 6 https://orcid.org/0000-0003-2874-1196

Tuan Do https://orcid.org/0000-0001-9554-6062

Jessica R. Lu https://orcid.org/0000-0001-9611-0009

Mark R. Morris https://orcid.org/0000-0002-6753-2066

Andrea M. Ghez https://orcid.org/0000-0003-3230-5055 Jay Anderson https://orcid.org/0000-0003-2861-3995

References

```
Anderson, J., & King, I. R. 2006, PSFs, Photometry, and Astronomy for the
   ACS/WFC, Tech. Rep., ACS 2006-01, Space Telescope Science Institute
Anderson, J., Sarajedini, A., Bedin, L. R., et al. 2008, AJ, 135, 2055
Anderson, L. D., Sormani, M. C., Ginsburg, A., et al. 2020, ApJ, 901, 51
Antonini, F., Capuzzo-Dolcetta, R., Mastrobuono-Battisti, A., & Merritt, D.
  2012, ApJ, 750, 111
Arca Sedda, M., Gualandris, A., Do, T., et al. 2020, ApJL, 901, L29
Arenou, F., Luri, X., Babusiaux, C., et al. 2018, A&A, 616, A17
Armillotta, L., Krumholz, M. R., & Di Teodoro, E. M. 2020, MNRAS,
   493, 5273
Armillotta, L., Krumholz, M. R., Di Teodoro, E. M., & McClure-Griffiths, N. M.
  2019, MNRAS, 490, 4401
Astropy Collaboration, Price-Whelan, A. M., Sipőcz, B. M., et al. 2018, AJ,
   156, 123
Astropy Collaboration, Robitaille, T. P., Tollerud, E. J., et al. 2013, A&A,
   558, A33
Bellini, A., Anderson, J., Bedin, L. R., et al. 2017, ApJ, 842, 6
Bellini, A., Libralato, M., Bedin, L. R., et al. 2018, ApJ, 853, 86
Binney, J., Gerhard, O. E., Stark, A. A., Bally, J., & Uchida, K. I. 1991,
   MNRAS, 252, 210
Binney, J., & Tremaine, S. 2008, Galactic Dynamics (2nd ed.; Princeton, NJ:
   Princeton Univ. Press)
Bitran, M., Alvarez, H., Bronfman, L., May, J., & Thaddeus, P. 1997, A&AS,
   125, 99
Bland-Hawthorn, J., & Gerhard, O. 2016, ARA&A, 54, 529
Böker, T., Falcón-Barroso, J., Schinnerer, E., Knapen, J. H., & Ryder, S. 2008,
   AJ, 135, 479
Bovy, J. 2015, ApJS, 216, 29
Buchner, J., Georgakakis, A., Nandra, K., et al. 2014, A&A, 564, A125
Butterfield, N., Lang, C. C., Morris, M., Mills, E. A. C., & Ott, J. 2018, ApJ,
  852, 11
Chatzopoulos, S., Fritz, T. K., Gerhard, O., et al. 2015, MNRAS, 447, 948
Clark, J. S., Lohr, M. E., Najarro, F., Dong, H., & Martins, F. 2018a, A&A,
   617, A65
Clark, J. S., Lohr, M. E., Patrick, L. R., et al. 2018b, A&A, 618, A2
Clarkson, W. I., Ghez, A. M., Morris, M. R., et al. 2012, ApJ, 751, 132
Cotera, A. S., Colgan, S. W. J., Simpson, J. P., & Rubin, R. H. 2005, ApJ,
  622, 333
Dame, T. M., Hartmann, D., & Thaddeus, P. 2001, ApJ, 547, 792
Do, T., Hees, A., Ghez, A., et al. 2019, Sci, 365, 664
Englmaier, P., & Gerhard, O. 1999, MNRAS, 304, 512
Espinoza, P., Selman, F. J., & Melnick, J. 2009, A&A, 501, 563
Feroz, F., & Hobson, M. P. 2008, MNRAS, 384, 449
Feroz, F., Hobson, M. P., & Bridges, M. 2009, MNRAS, 398, 1601
Figer, D. F., Kim, S. S., Morris, M., et al. 1999a, ApJ, 525, 750
Figer, D. F., McLean, I. S., & Morris, M. 1999b, ApJ, 514, 202
Figer, D. F., Najarro, F., Gilmore, D., et al. 2002, ApJ, 581, 258
Gaia Collaboration, Brown, A. G. A., Vallenari, A., et al. 2021, A&A, 649, A1
Gaia Collaboration, Prusti, T., de Bruijne, J. H. J., et al. 2016, A&A, 595, A1
Gallego-Cano, E., Schödel, R., Nogueras-Lara, F., et al. 2020, A&A, 634, A71
Gerhard, O. 2001, ApJL, 546, L39
Gerhard, O., & Martinez-Valpuesta, I. 2012, ApJL, 744, L8
Gravity Collaboration, Abuter, R., Aimar, N., et al. 2022, A&A, 657, L12
Hankins, M. J., Lau, R. M., Morris, M. R., & Herter, T. L. 2017, ApJ, 837, 79
Henshaw, J. D., Longmore, S. N., Kruijssen, J. M. D., et al. 2016, MNRAS,
   457, 2675
```

```
Hosek, M. W., Jr., Lu, J. R., Anderson, J., et al. 2015, ApJ, 813, 27
Hosek, M. W., Jr., Lu, J. R., Anderson, J., et al. 2018, ApJ, 855, 13
Hosek, M. W., Jr., Lu, J. R., Anderson, J., et al. 2019, ApJ, 870, 44
Hunter, J. D. 2007, CSE, 9, 90
Hußmann, B., Stolte, A., Brandner, W., Gennaro, M., & Liermann, A. 2012,
   A&A, 540, A57
Kim, S. S., Figer, D. F., Lee, H. M., & Morris, M. 2000, ApJ, 545, 301
Kim, S. S., & Morris, M. 2003, ApJ, 597, 312
Kim, S. S., Morris, M., & Lee, H. M. 1999, ApJ, 525, 228
Krieger, N., Ott, J., Beuther, H., et al. 2017, ApJ, 850, 77
Kruijssen, J. M. D., Dale, J. E., & Longmore, S. N. 2015, MNRAS, 447, 1059
Kruijssen, J. M. D., Dale, J. E., Longmore, S. N., et al. 2019, MNRAS,
  484, 5734
Lang, C. C., Goss, W. M., & Morris, M. 2001, AJ, 121, 2681
Lang, C. C., Goss, W. M., & Wood, O. S. 1997, ApJ, 474, 275
Langer, W. D., Velusamy, T., Morris, M. R., Goldsmith, P. F., & Pineda, J. L.
  2017, A&A, 599, A136
Launhardt, R., Zylka, R., & Mezger, P. G. 2002, A&A, 384, 112
Lenzen, R., Hartung, M., Brandner, W., et al. 2003, Proc. SPIE, 4841, 944
Libralato, M., Fardal, M., Lennon, D., van der Marel, R. P., & Bellini, A. 2020,
   MNRAS, 497, 4733
Liermann, A., Hamann, W.-R., & Oskinova, L. M. 2009, A&A, 494, 1137
Liermann, A., Hamann, W.-R., & Oskinova, L. M. 2012, A&A, 540, A14
Lindegren, L., Klioner, S. A., Hernández, J., et al. 2021, A&A, 649, A2
Longmore, S. N., Kruijssen, J. M. D., Bally, J., et al. 2013, MNRAS,
  433, L15
Martins, F., Hillier, D. J., Paumard, T., et al. 2008, A&A, 478, 219
Molinari, S., Bally, J., Noriega-Crespo, A., et al. 2011, ApJL, 735, L33
Morris, M., & Serabyn, E. 1996, ARA&A, 34, 645
Najarro, F., Figer, D. F., Hillier, D. J., & Kudritzki, R. P. 2004, ApJL,
  611, L105
Oliphant, T. E. 2006, A Guide to NumPy, Vol. 1 (USA: Trelgol Publishing)
Portegies Zwart, S. F., Makino, J., McMillan, S. L. W., & Hut, P. 2002, ApJ,
Reid, M. J., & Brunthaler, A. 2004, ApJ, 616, 872
Reid, M. J., & Brunthaler, A. 2020, ApJ, 892, 39
Ridley, M. G. L., Sormani, M. C., Treß, R. G., Magorrian, J., & Klessen, R. S.
  2017, MNRAS, 469, 2251
Rodriguez-Fernandez, N. J., & Combes, F. 2008, A&A, 489, 115
Rousset, G., Lacombe, F., Puget, P., et al. 2003, Proc. SPIE, 4839, 140
Rui, N. Z., Hosek, M. W. J., Lu, J. R., et al. 2019, ApJ, 877, 37
Salas, J. M., Naoz, S., & Morris, M. R. 2020, arXiv:2010.04170
Schödel, R., Feldmeier, A., Kunneriath, D., et al. 2014, A&A, 566, A47
Schönrich, R., Binney, J., & Dehnen, W. 2010, MNRAS, 403, 1829
Schwarz, G. 1978, AnSta, 6, 461
Simpson, J. P., Colgan, S. W. J., Cotera, A. S., et al. 2007, ApJ, 670, 1115
Sofue, Y. 1995, PASJ, 47, 527
Sormani, M. C., Magorrian, J., Nogueras-Lara, F., et al. 2020a, MNRAS,
Sormani, M. C., Sanders, J. L., Fritz, T. K., et al. 2022, MNRAS, 512, 1857
Sormani, M. C., Tress, R. G., Glover, S. C. O., et al. 2020b, MNRAS,
  497, 5024
Sormani, M. C., Treß, R. G., Ridley, M., et al. 2018, MNRAS, 475, 2383
Stolte, A., Ghez, A. M., Morris, M., et al. 2008, ApJ, 675, 1278
Stolte, A., Hußmann, B., Morris, M. R., et al. 2014, ApJ, 789, 115
Stolte, A., Hußmann, B., Olczak, C., et al. 2015, A&A, 578, A4
Støstad, M. N., Do, T., Murray, N., et al. 2015, ApJ, 808, 106
Tress, R. G., Sormani, M. C., Glover, S. C. O., et al. 2020, MNRAS, 499, 4455
Virtanen, P., Gommers, R., Oliphant, T. E., et al. 2020, NatMe, 17, 261
Wang, Q. D., Dong, H., Cotera, A., et al. 2010, MNRAS, 402, 895
Wang, Q. D., Dong, H., & Lang, C. 2006, MNRAS, 371, 38
Wegg, C., & Gerhard, O. 2013, MNRAS, 435, 1874
```